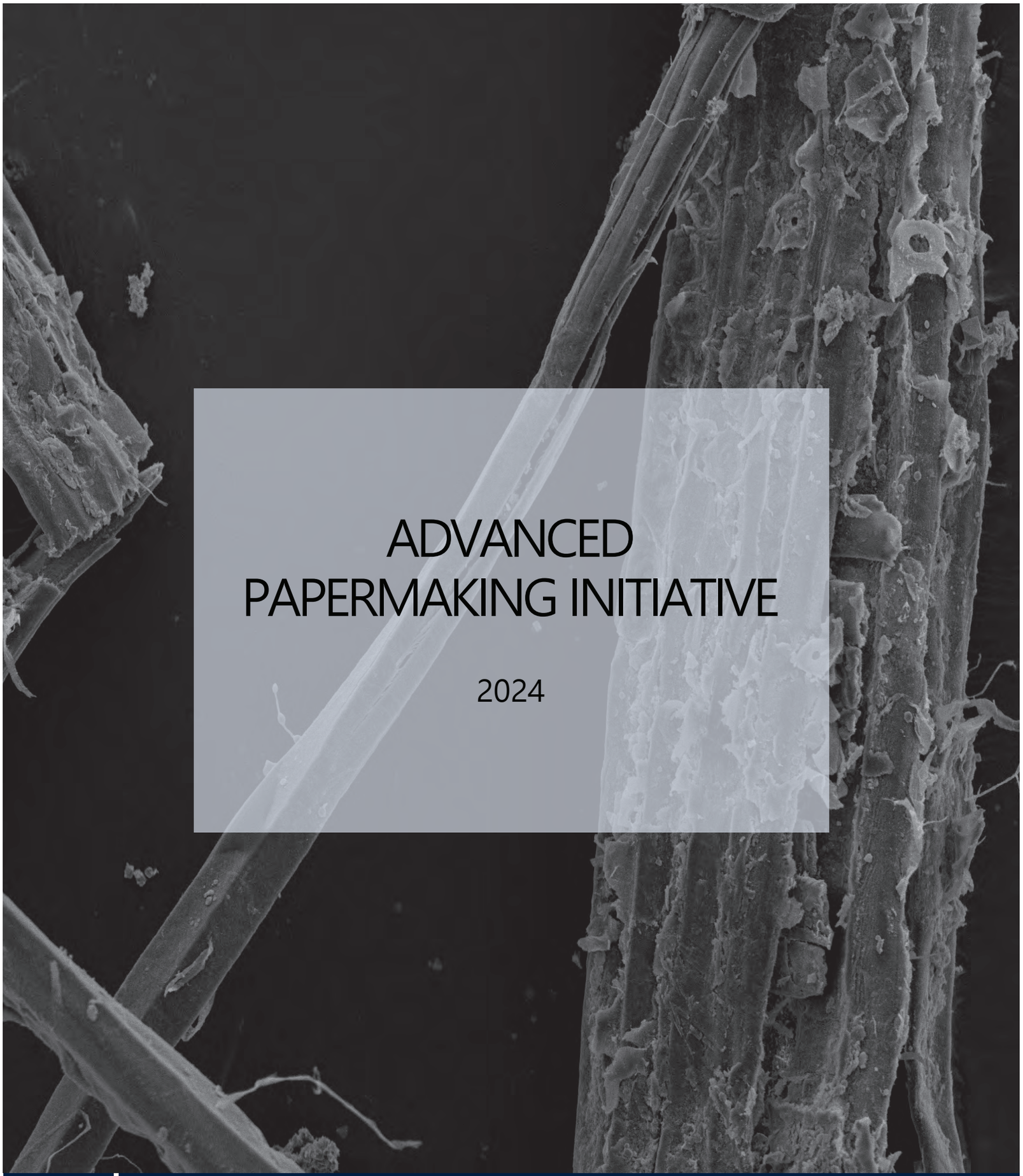

ADVANCED PAPERMAKING INITIATIVE

2024

THE UNIVERSITY OF BRITISH COLUMBIA

WELCOME MESSAGE

Dear reader:

We are excited to share with you our latest research report as part of the Advanced Papermaking Initiative (API).

For this report we have focused on summarizing the research progress of the past year of the Energy Reduction in Mechanical Pulping (ERMP) consortium.

We invite you to read the following pages to gain an understanding of the eight projects of the current Phase 3 of the ERMP program. Each one of these projects have been reviewed during our last Steering Committee meeting held in the UBC campus early this month with university and industry participation.

Sincerely,

Ph.D., P. Eng.,
Professor of Chemical and Biological Engineering, UBC
Principal Investigator, ERMP Research Program

CONTRIBUTORS

Matthias Aigner
Rodger Beatson
Samuel Brown
Emily Cranston
James Drummond
Elisa Ferreira
Mariana Frias de Albuquerque
Siddharth Groove
Mark Martinez
Lewis Mason
Gloria Noki
Kudzanai Nyamayaro
James Olson
André Phillion
Scott Renneckar
Norman Roberts
Laurel Schafer
Boris Stoeber
Heather Trajano
Daniela Vargas Figueroa
Anderson Veiga
Yimin Wang
Peter Wild
Adam Wu
Fariba Yeganeh
Cameron Zheng

DESIGNER CONTACT
Program Manager
Daniela Vargas Figueroa
daniela.figueroa@ubc.ca
604-827-2390

UBC Pulp and Paper Centre
2385 East Mall Vancouver, BC V6T 1Z4

CONTENTS

RESEARCH UPDATES

System design, Sensors and Control

4 **PROJECT 1.1** - LC refining of mechanical pulp.

8 **PROJECT 1.2** - Data-driven control and analytics in the pulp and paper industry.

12 **PROJECT 1.3** - Creating low-energy shive-free pulps.

Valorization of TMP fines

15 **PROJECT 2.1** - Lignin-rich fines: Simple routes towards creation of hydrophobic and hydrophilic filler additives.

19 **PROJECT 2.2** - From trees to treatment: Functionalizing TMP extractives.

23 **PROJECT 2.3** - Production, characterization, and applications of MFC-derived from mechanical pulp fines.

27 **PROJECT 2.3B** - Incorporating microfibrillated cellulose for high strength and high bulk

New Product Development

30 **PROJECT 3.1** - Chemical modification and advanced characterization of fibres

33 **PROJECT 3.2** - Advanced characterization - X-ray computed tomography

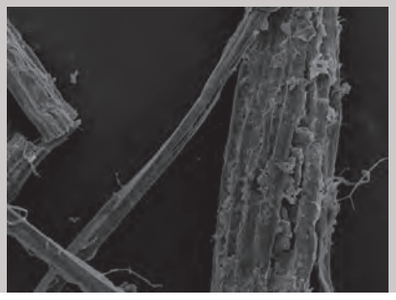

ON THE COVER

Secondary Refined TMP fibre treated with iron (II) sulfate and sodium hydroxide. The image was obtained using secondary electrons mode in SEM. Author - Anderson de Veiga.

PROJECT 1.1

LC REFINING OF MECHANICAL PULP

Authors: Matthias Aigner, Mark Martinez, James Olson, Peter Wild

Background

In previous research conducted by the University of Victoria, a custom piezo-ceramic force sensor was developed to measure local shear and normal forces on refiner bars. This sensor design has been utilized in various trials, including high consistency (HC) refiners [Olender et al. 2008] and low consistency (LC) refiners [Harirforoush et al. 2018]. Recent trials at the Pulp and Paper Centre at UBC and the Catalyst, Paper Excellence mill in Crofton, BC, aimed to investigate the influence of operating conditions on the radial distribution of bar forces during bar-passing events [Aigner et al. 2020, Aigner et al. 2022]. This research has led to new questions, particularly regarding the impact of plate geometry on the refining process. Current studies focus on how plate geometry parameters, such as bar width and bar edge length (BEL), affect how power is expended during the refining process, in the context of LC refining.

Methods

As discussed in a previous newsletter update, a method has been established to measure key plate parameters from images, drawing inspiration from the work of Elahimehr et al. [Elahimehr et al. (2015)]. This process is delineated in Figure 1. Utilizing high-resolution coloured images of the refiner plates (Figure 1 (a)), binary images are generated for the rotor side and the stator side (Figure 1 (b) and 1 (c)). These binary images are then used to identify the areas of overlap between the stator bars and the rotor bars (Figure 1 (d)). The geometry of these overlap areas is used as the basis for new plate geometry parameters, i.e., size and radial location of each overlap area, number of overlap areas, and edge length of each overlap area.

A model to estimate net refiner power, P, was developed, based on the measured forces and overlap areas. The power expended at a given overlap area, P_i, is estimated as shown in Equation 1:

$$P_i = \tau A_i r_i \omega \quad (1)$$

A_i is the size of the overlap area; r_i is the radial position of the overlap area; ω is rotational speed; τ is the tangential shear stress at the overlap area. Net refiner power is then estimated as the sum of the power expended at each of the overlap areas, as shown in Equation 2:

$$P = \sum_{i=1}^{N_c} \tau A_i r_i \omega \quad (2)$$

In this equation: N_c is the number of overlap areas. It is assumed that shear stress, τ, does not vary among the contact areas due to the relatively small radial span of the refining zone (i.e., 0.12 m to 0.19 m). This shear stress is determined based on force sensor measurements following Equation 3.

$$\tau = \frac{F_s}{A_s} \quad (3)$$

In this equation, F_s is the mean shear force measured by the force sensor and A_s is the area size of the force sensor.

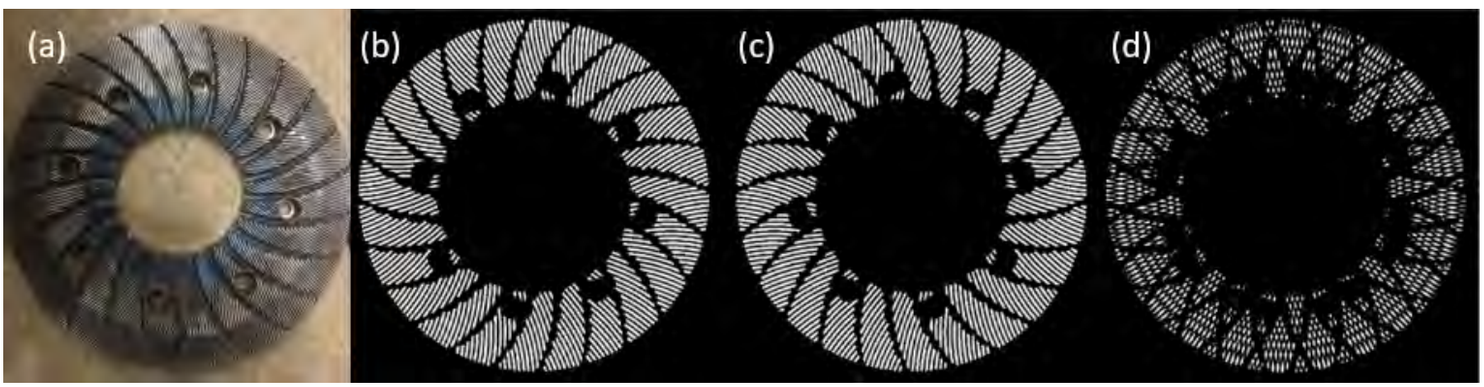

Figure 1. Plate geometry pipeline. (a) Picture of a refiner plate. (b) Black and white image of a stator plate (c) and a rotor plate. (d) Bar interaction area image generated using (b) and (c).

PROJECT 1.1

Results

Plate geometry

An analysis of the trends for the overlap area size is presented in Figure 2 and Figure 3. Comparing the scaled scatter plots of the overlap area size, plotted against the radial position for the three plates, P1, P2 and P3, unveils both differences and similarities between these plates.

All three plates show a similar characteristic shape in the scatter plots of the overlap area, namely, two clusters of data points, one ranging from a radius of 0.11 to 0.16 m and a second ranging from 0.14 to 0.19 m. Each cluster exhibits increasing overlap area size with increasing radius. For each plate, the second cluster overlaps the first cluster and the second cluster rises to the maximum overlap area size close to the plate periphery.

The principal difference among the three plates is the maximum value of overlap area size. P3 shows the highest values while P2 and P1 feature a maximum overlap area size that is less than half that of P3. This effect is attributed to bar width differences. P3 has a bar width of 2.5mm while P1 and P2 both have a bar width of 1.4mm.

To investigate the distribution of overlap area size with radial position, two-dimensional histogram plots are presented in Figure 3. To generate these plots the radius and overlap area size ranges are each split into 20 equal-sized ranges, resulting in a 20x20 grid for each plate. This grid is used to sort all overlap areas into bins based on their respective overlap area size and the location of their centroid. The number of overlap areas falling into each bin range is summed up and indicated in colour in the plots.

The histogram plots in Figure 3 highlight, similar to the plots in Figure 2, the differences in the pattern of overlap areas among the three plates. Furthermore, these plots show which plate has the greatest number of overlap areas at a given area size and radial position. This plate is P2 with 100 overlap areas at a radius of 0.175 m and an area size of 6 mm2 and P2 has the highest number of overlap areas between the plates. P2 is the plate with the highest value of BEL at 5.2 km/rev while P1 and P3 have a BEL of 2.1 km/rev. This indicates that a high BEL can be an indicator of a high number of overlap areas.

All three plates show the highest overlap area counts in the second cluster, between a radius of 0.15 and 0.18 m. Also, Figure 3 shows, that the number of small overlap areas (i.e., < 0.5 mm^2) is high through the full radius range.

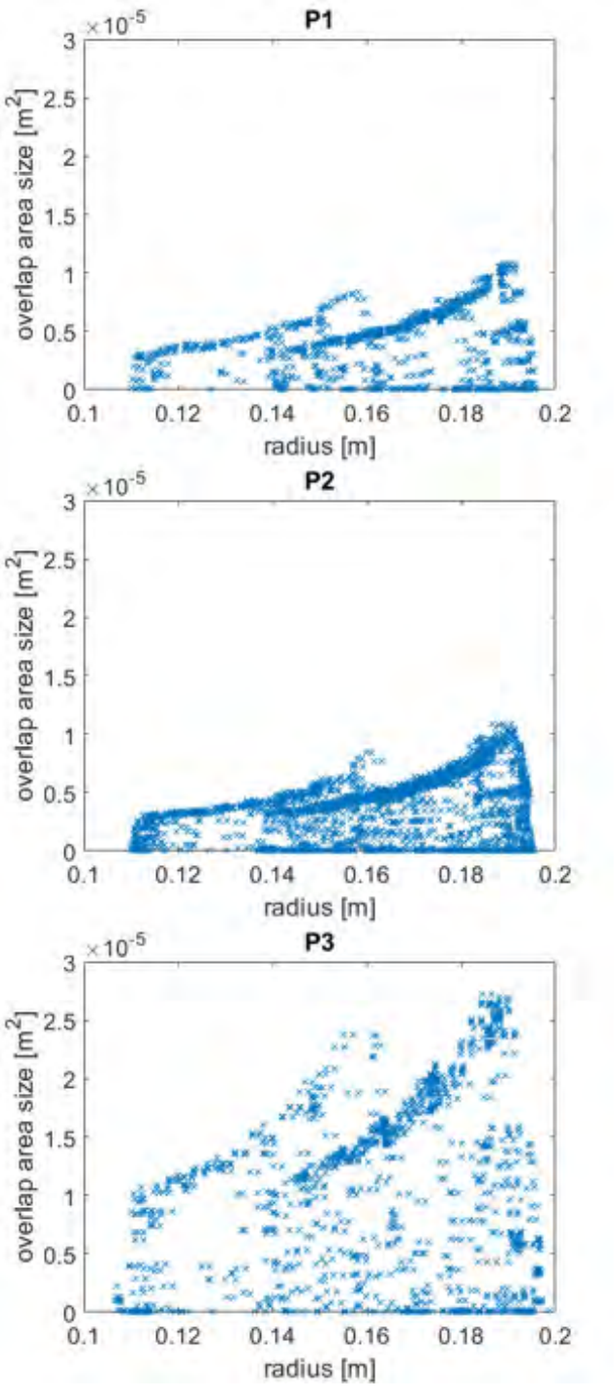

Figure 2. Overlap area size versus radius for three stator and rotor plate patterns. P1, P2, and P3 indicate the respective plate patterns.

PROJECT 1.1

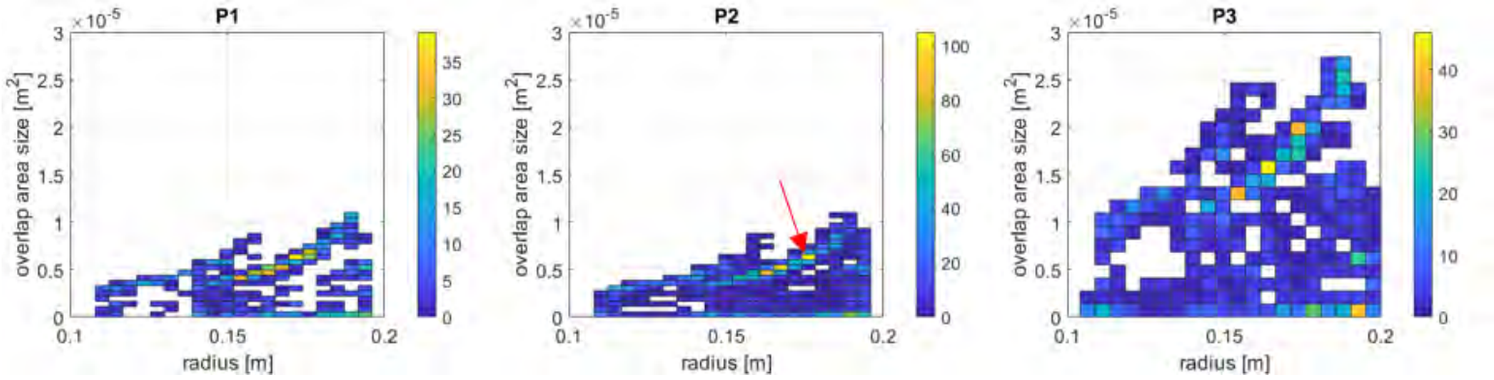

Figure 3. Two-dimensional histogram plots with overlap area size and radius as the two dimensions. Color bars indicate the number of overlap areas within each bin. P1, P2, P3 indicate the respective plates.

In Figure 4, the overlap areas are binned as in Figure 3, but instead of counting the number of overlap areas in each bin, the power for each overlap area in each bin is calculated, using Equation 1, and then the sum of all powers of all overlap areas in each bin is produced. This combined power for each bin is displayed instead of the number of overlap areas for each in. In this way, the colour coding in Figure 4 shows at which radial position and at what overlap area size the most amount of power is expended.

The plate with the most power expended at any one bin is P2 with 0.7 kW at a radius of 0.175 m and an area size of 6 mm². This the also the location where the greatest number of overlap areas was recorded, as shown in Figure 3c.

For all three plates, more power is expended in the second cluster than in the first. The great number of overlap areas in the below 0.5 mm² range becomes insignificant when considering the power expended at these overlap areas.

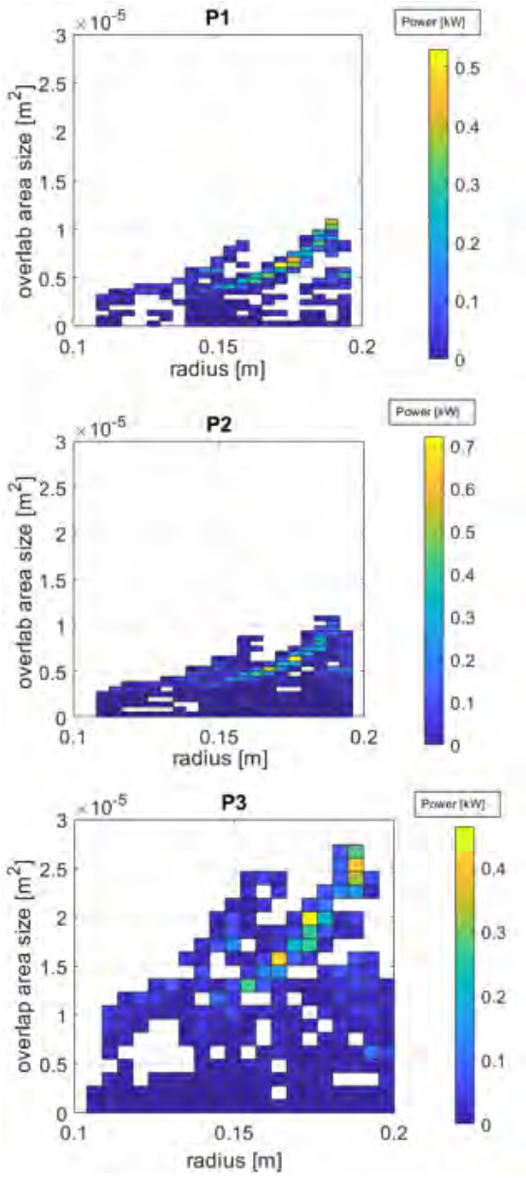

Figure 4. Two-dimensional histogram of power versus overlap area size and radius. Colour indicates the expended power. P1, P2, P3 indicate the respective plates.

PROJECT 1.1

Force estimate

Similar to the calculation of power for each overlap area, based on the force sensor measurements, the mean force per overlap area can be estimated based on power measurements. In Figure 5, this estimated mean force is plotted against the actual mean measured force for previously completed trials [Aigner et al. 2023]. Each data point is based on a recirculation trial with the measured force representing the mean force of the respective trial. The refiner plate and the rotational speed are indicated in the legend.

Figure 5 shows that the estimates of mean force per overlap area are in reasonably good agreement with the mean measured refiner bar force. In most cases, the calculated mean shear force is greater than the measured mean shear force. Out of 18 trials, the calculated force disagrees with the measured force in three trials more drastically. In these cases, the recorded mean shear forces do not represent the power level of the respective trial. All three trials are high-power trials (<35kW). The authors assume that a change in the shape of the force profile results in a lower-than-expected mean shear force.

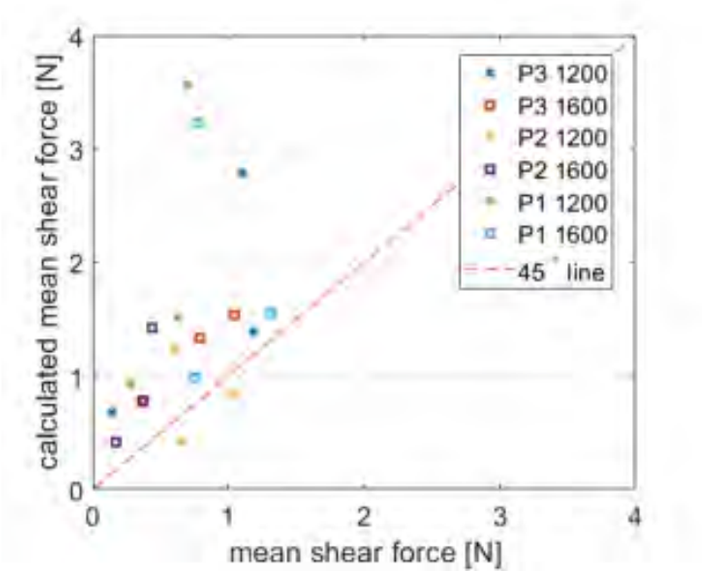

Figure 5. Calculated mean shear forces plotted against measured mean shear force.

References

1. Aigner, M., Olson, J., and Wild, P. (2020). Measurement and interpretation of spatially registered bar-forces in LC refining. Nordic Pulp & Paper Research Journal, 35(4), 600-610.
2. Aigner, M., Olson, J., Sun, Y., and Wild, P. (2022). Interpretation of force profiles in mill-scale LC refining. Nordic Pulp & Paper Research Journal, 37(1), 42-53.
3. Aigner, M., Gharehkhani, S., Martinez, M., Olson, J., and Wild, P. (2023). Project 1.1: LC Refining of Mechanical Pulp. Energy reduction in mechanical pulping – November 2023- Newsletter, p4-8.
4. Elahimehr, A., Olson, J. A. and Martinez, D. M. (2015): Low consistency refining of mechanical pulp: how plate pattern and refiner operating conditions change the final properties of pulp, Nord. Pulp Pap. Res. J., 30(4), 609–616.
5. Harirforoush, R, Olson, J., and Wild, P. (2018). In-Process Detection of Fiber Cutting in Low Consistency Refining Based on Measurement of Forces on Refiner Bars. Tappi Journal 16 (4): 460–69.
6. Olender, D., Wild, P., & Byrnes, P. (2008). A piezoelectric force sensor for mill-scale chip refiners. Proceedings of the Institution of Mechanical Engineers, Part E: Journal of Process Mechanical Engineering, 222(2), 115-122.

Acknowledgements

The authors thank Mr. Norm Roberts for conducting the refining trials and the co-op students at the UBC-PPC for their hard work in analysing the fibre data.

PROJECT 1.2

DATA-DRIVING CONTROL AND ANALYTICS IN THE PULP AND PAPER INDUSTRY

Authors: Siddharth Grover, Bhushan Gopaluni, Yankai Cao

Background

Mechanical pulping is a process that converts lignocellulosic materials into pulp by using mechanical energy i.e. with reduced use of chemicals. In the context of modern manufacturing, the production process is highly complex and benefits from being data-driven. The primary focus has traditionally been on maximizing output and efficiency while minimizing downtime and production lags (Yin et. al., 2023). However, with the recent shift towards sustainability, there is an additional layer of complexity that impacts process improvement.

The introduction of advanced analytics and AI methodologies has been a transformative change for the pulp and paper industry. These technologies are not just tools for improving efficiency, but also essential for achieving a deeper understanding of the production processes and their nuances. By analyzing large amounts of data in real time, AI and ML models can identify anomalies that are not immediately apparent to human operators, and monitor the production process. From sensor data, AI models can predict when maintenance is required, preventing costly and disruptive unplanned downtime (Blomqvist, 2020).

The end goal of leveraging AI and ML in this setting is not just to streamline operations but to also enhance the sustainability of the manufacturing processes. By optimizing energy use, AI and ML contribute directly to lowering the industry's carbon footprint, which aligns with global efforts to create more sustainable industries. These technological advancements push the needle forward for what can be achieved in manufacturing, and define new benchmarks for efficiency, quality, and environmental responsibility.

Progress Summary

Previously, the project focused on building a deep learning policy-based model predictive control system. This was accompanied by an exploratory data analysis (EDA) to understand the variables and their relationships with each other. However, a novel solution is being engineered, which is currently the focus of the project.

Exploratory Data Analysis

Initially, an extensive exploratory data analysis phase is carried out to identify relationships amongst variables, interesting patterns, and anomalies in production patterns or key performance indicators - this helps characterize gigabytes of production data with just a few key insights. This uses simple methods such as Pearson correlation, time series analysis, statistical independence tests, and visuals such as density plots, heat maps, scatter plots, and box plots.

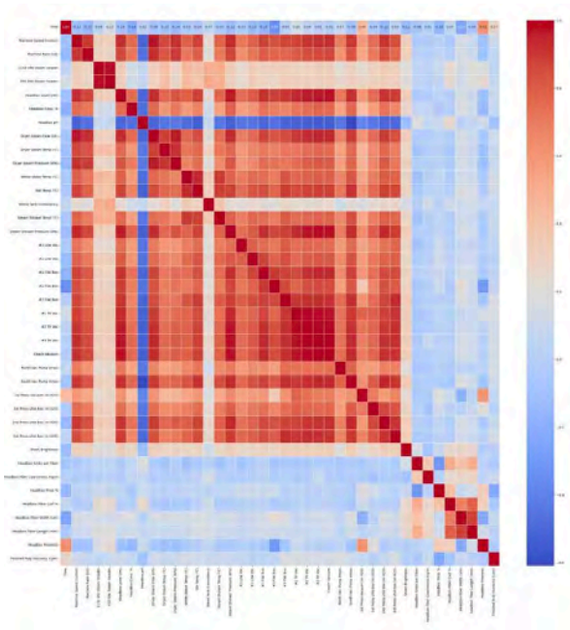

Figure 1. Correlation matrix of machine variables.

Results from this stage are being analyzed to identify anomalies within the production process as well as important variables.

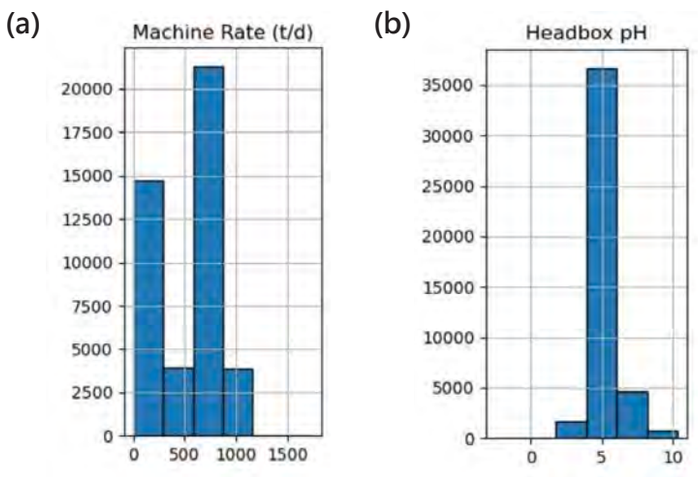

Figure 2. Histogram of (a) machine production rate and (b) Headbox pH, two variables with the most negative correlation

PROJECT 1.2

Proposed Methodology and Progress

The project aims to identify which part of the process (i.e. features) are contributing to production inefficiencies and losses, while also leading to higher energy consumption, with the stretch goal of building a causal network (directed acyclic graph) between production variables. Additionally, another objective is to build a predictive model for production rate or production losses, or identifying periods of low efficiency. The ultimate objective is to build an automated production planning system - trained through deep reinforcement learning methods such as Q-learning. Throughout this procedure, these models will be tested in industrial settings.

To achieve these goals, a variety of methods are considered and the best are developed further. The first part of the project (feature selection) is addressed majorly using EDA and ML models; the second part (predictive model) through deep learning methods (which can capture complex patterns that ML models cannot); and the third part (production planning system) through reinforcement learning and optimization.

Machine Learning for Identifying Key Causes of Production Rate Decline: To advance beyond traditional analysis techniques, the project incorporates several machine learning models to enhance predictive capabilities and process control:

Tree-based learners (Fleyeh, Hansson, Yella, 2016): Utilizing Random Forest algorithm and eXtreme Gradient Boosting, the aim is to improve predictive accuracy by selecting the most important process variables. In the pulp and paper industry, these models are crucial for identifying critical variables, such as fiber moisture content and pulp density, which significantly impact production efficiency and paper quality. XGBoost develops one tree at a time, leading to slightly better results than random forest. The prediction from a Random Forest model is the average of the predictions from all decision trees:

$$[\hat{y} = \frac{1}{B} \sum_{b=1}^{B} T_b(x)]$$

where *B* is the number of trees, T_b is the prediction of the b-th tree, and *x* is the input feature vector. The model update in XGBoost, using the gradient boosting framework, is given by:

$$[\hat{y}_i^{(t+1)} = \hat{y}_i^{(t)} + \eta \cdot \sum_{k=1}^{K} f_k(x_i)]$$

where $\hat{y}_i^{(t)}$ is the prediction at iteration t, f_k is the k-th tree, K is the number of boosting rounds, x_i is the feature vector for instance i, and *n* is the learning rate.

Partial Least Squares Regression (PLSR) (Huang et. al., preprint): This method is most useful for dealing with multicollinearity and high-dimensional data, such as with the pulp and paper data, to select the most important features. PLSR projects the predictor variables X and the response variables Y to a new space and performs linear regression in that space:

$$[T = XW, \quad U = YQ, \quad T \approx U]$$

where T and U are the matrices of the latent variables for X and Y respectively, and W and Q are the loading matrices.

Causal Bayesian Networks (CBN) for Enhanced Process Control in Pulp Mills

Causal Bayesian Networks serve as decision support tools by allowing simulation of different scenarios and their impacts on the network. For example, CBNs can predict how adjustments in the wood chip refinement process, steam pressure, or chip meter speed affect the overall production rate and energy consumption. By manipulating input variables in the network, changes in the production rate can be observed. This can guide decision-making in terms of resource allocation, maintenance scheduling, or operational changes aimed at optimizing productivity and sustainability. Additionally, by analyzing the network's conditional probabilities and the observed data, the most likely cause of the anomalies can be inferred.

The backbone of a Causal Bayesian Network is its ability to model joint probability distributions. In the case of a pulp mill, the network structure is likely unknown due to a variety of variables. The joint probability of a Bayesian network can be decomposed into:

$$[P(x_1, x_2, \ldots, x_n) = \prod_{i=1}^{n} P(x_i \mid \mathrm{Pa}(x_i))]$$

PROJECT 1.2

Where Pa (x_i) denotes the parents of node i in the graph. The graph structure is determined using a variety of methods, with the most common being Max-Min Hill-Climbing algorithm, which seeks to maximize the mutual information shared between two variables given a known set Z (objective function), as well as minimizing the size of set Z given the variable pairs earlier.

Attention-based Deep Learning: A Novel Application

The integration of deep learning techniques focuses on capturing and modeling temporal dynamics, complex interactions, and non-linearities that simpler models might not pick up on. One such model, known as a transformer, has been gaining attention.

Transformers use a mechanism called "self-attention" to process all parts of the input data in parallel, while focusing on the important parts. The self-attention mechanism in a Transformer model is computed as:

$$[\text{Attention}(Q, K, V) = \text{softmax}\left(\frac{QK^T}{\sqrt{d_k}}\right)V]$$

where Q, K, and V are the query, key, and value matrices derived from the input, and d_k is the dimensionality of the keys. This allows transformers to handle long-range dependencies more effectively and efficiently.

The transformer model consists of an encoder and a decoder, each made up of multiple layers of self-attention and position-wise feed-forward networks (FFN). This allows them to detect subtle patterns and dependencies between different stages of the manufacturing process (Kavasidis et. al., 2023).

For example, readings of chip meter speed, refiner load, and production rate can be used to predict potential breakdowns or quality issues before they occur. By processing all these data points in parallel and understanding their complex relationships, transformers (like other neural networks) can predict when maintenance should be performed, or what conditions lead to that state. Additionally, if a deviation in moisture content (or another variable) is detected in the process, a transformer can predict its impact on the final paper quality and suggest adjustments to the drying parameters or chemical additives to compensate for the deviation. Finally, by analyzing the sequence of energy consumption data alongside production output data, a transformer can identify patterns and suggest optimal operating conditions that reduce energy usage without compromising output quality (Mateus et. al., 2022).

Conclusion and Future Work

The project continues to push the boundaries of what can be achieved in the pulp and paper industry through the integration of advanced analytics, machine learning, and deep learning technologies.

After implementing the aforementioned models, and inferring their results, additional objectives will be set as forward-looking tasks.

Real-Time Analytics Implementation: This will allow for immediate feedback and adjustments, allowing for a prepared response to anomalies and downtime.

Interactive Dashboard: A visual, interactive dashboard will serve as a central hub for accessing real-time insights and historical data analysis. This will contain production and planning information most relevant to plant operators, managers, as well as other key stakeholders.

Deep Reinforcement Learning for Production Planning and Predictive Maintenance: Production environments in industries like pulp and paper are dynamic, with frequent changes in demand, supply chain issues, and varying operational conditions. DRL's ability to adapt its strategy in response to environmental changes without human intervention makes it an excellent tool. DRL focuses on maximizing cumulative rewards over time, making it ideal for pulp mill production planning where short-term decisions can have significant long-term impacts.

For example, in a pulp mill, rewards can be structured around production output but also energy consumption, resource utilization, quality, downtime, and maintenance costs. This tailored approach makes DRL a viable solution for specific, customized goals that meet the needs of the several ERMP partners.

PROJECT 1.2

References

1. Yin, L., Liang, X., Wang, R., Liu, K., & others. (2023). Development of Raw Materials and Technology for Pulping—A Brief Review. Polymers, 15(22), 4465. https://doi.org/10.3390/polym15224465
2. Blomqvist, A. (2020, March 16). Artificial intelligence and machine learning enable major savings in the pulp and paper industry. TietoEVRY. Retrieved from https://www.tietoevry.com
3. Fleyeh, H., Hansson, K., & Yella, S. (2016). Feature Selection and Bleach Time Modelling of Paper Pulp Using Tree Based Learners. In Proceedings of the Web Information Systems Engineering – WISE 2016 (pp. 385-396). Springer. https://doi.org/10.1007/978-3-319-48743-4_31
4. Comprehensive model optimization in pulp quality prediction: a machine learning approach by Chin-Wei Huang, Luc Baron, Marek Balazinski, and Sofiane Achiche, Department of Mechanical Engineering, École Polytechnique de Montréal, Montréal, Québec, Canada. Available online at https://peerj.com/preprints/2749.pdf. (NOTE: NOT PEER REVIEWED)
5. Kavasidis, I., Lallas, E., Gerogiannis, V. C., Charitou, T., & Karageorgos, A. (2023). Predictive maintenance in pharmaceutical manufacturing lines using deep transformers. Procedia Computer Science, 220, 576-583. https://doi.org/10.1016/j.procs.2023.01.073
6. Mateus, B. C., Mendes, M., Farinha, J. T., Cardoso, A. M., Assis, R., & Soltanali, H. (2022). Improved GRU prediction of paper pulp press variables using different pre-processing methods. Cognition Technology & Work, Article 2155263. https://doi.org/10.1080/21693277.2022.2155263

PROJECT 1.3

CREATING LOW-ENERGY SHIVE-FREE PULPS

Authors: Rodger Beatson, Heather Trajano, Gloria Noki, L. Tran, M. Chen, N. Jalali

Background

The objectives of this project are to: (1) generate an understanding of the impact chemical treatments have on the development of fibre and fines' properties during LC refining, and (2) develop economically viable low-energy processes that combine such treatments with LC refining to produce printing/writing, board and packaging grades.

Previous work by Chang et al. (2016) compared the effects of alkaline peroxide, chlorine dioxide, and ozone treatments with subsequent LC refining on TMP. Results showed that introducing oxidative agents reduces electrical energy consumption and improves pulp strength. Alkaline peroxide is hypothesized to generate acid groups on the surface of fibres and fines, increasing surface charge and causing surface fibre swelling. Swelling increases the bonded surface area and causes sheet densification. Chlorine dioxide and ozone are thought to oxidize lignin to produce carboxylic acids. A subsequent alkali soak forms sodium salt, which brings about the softening and swelling of fibres and fines, leading to an increase in tensile strength.

The current approach to advance highly alkaline peroxide treatment (HAPT) includes studying the kinetics of strength development and determining the contribution of fines to the property development of handsheets. The rate of increase in tensile strength during HAPT is hypothesized to be dependent on acid group generation and thus dependent on temperature, the concentration of hydroxide ion (pH) and the concentration of hydrogen peroxide. To provide a basis for the kinetic studies, we have determined how pH and hydrogen peroxide concentration change during HAPT in the presence of fines (whole pulp) and absence of fines (long fibres only). Furthermore, we have investigated the kinetics of acid group development in the fibre and fines.

Materials and Methods

Separation of Fibers and Fines

The secondary refiner TMP used in the HAPT study was provided by Holmen Braviken. Batches of 20 g OD pulp were hot disintegrated using standard procedures. Deionized (DI) water was added to achieve 0.5% consistency. The suspension was then placed in a 200-mesh basket. Constant agitation was applied using a Sommerville Shive agitator while 16 L of DI water was used to wash the suspension. Long fibres were retained in the 200-mesh sieve whereas the filtrate containing fines was collected in a bucket.

Kinetics of strength development in HAPT

Whole pulp and long fibres were each subjected to HAPT. The whole pulp contained 70% fines as determined by the Bauer McNett fibre classifier. The pulp or long fibres were chelated with a 0.2% charge diethylene triamine pentaacetic acid (DTPA) at 4% consistency at 60°C in a water bath for 30 minutes. The solids were washed with DI water. DI water was recirculated for the whole pulp trials in order to retain fines.

The chelated material was treated in a plastic bag with 4% H_2O_2, 6% NaOH, and 3% Na_2SiO_3 at 10% consistency at 65°C for 30, 60 and 120 minutes. Mixing was achieved by squeezing the bag every 5 minutes for the first 10 minutes, every 10 minutes for the next 20 minutes, and every 30 minutes for the remaining duration of the treatment. After treatment, the slurry was filtered and washed as described above.

The final pH and residual peroxide of the HAPT filtrate were measured. Residual peroxide was determined using iodometric titration with 0.1 N sodium thiosulfate as the titrant. Weak acid content was determined using conductometric titration (June 2022 Newsletter).

Handsheets were prepared according to TAPPI standard methods. Handsheet properties were determined according to TAPPI standards.

HAPT is currently being conducted at times less than 30 minutes; results will be available in the Steering Committee Meeting presentation.

PROJECT 1.3

Results

Final pH and residual peroxide

As time increases from 30 minutes to 60 minutes, the final pH increases and the peroxide residual decreases (Figures 1 and 2). The decrease in residual peroxide reflects peroxide decomposition and consumption through reaction with the pulp. Hydrogen peroxide is acidic forming the hydroperoxide ion with base, thus at lower peroxide contents the pH will be higher (June 2023 Newsletter).

When time increases from 60 minutes to 120 minutes, the long fibre filtrate pH continues to increase as peroxide concentration decreases. However, the whole pulp filtrate pH decreases despite the decreasing peroxide concentration. This pH drop may be attributed to the consumption of alkali by the high acid group content of whole pulp (Figure 5 for further discussion).

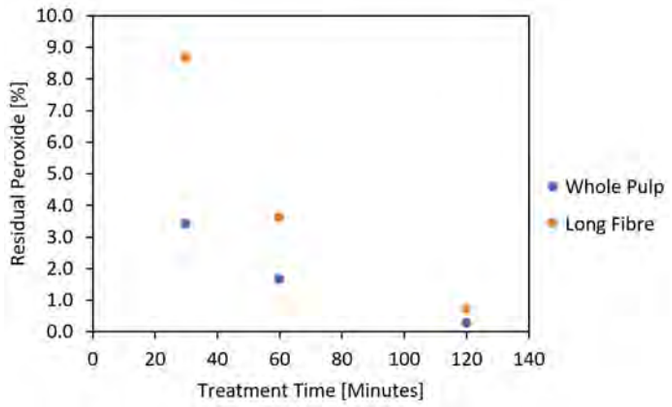

Figure 2. Percentage residual peroxide decreases over treatment time. The peroxide concentration drops rapidly during the first 30 minutes of HAPT.

Pulp properties

From 30 to 120 minutes, brightness decreases with treatment time (Figure 3). This decrease is attributed to the increased alkalinity resulting from peroxide consumption.

There are minimal tensile strength gains for whole pulp when the treatment time is extended beyond 30 minutes (Figure 4). The generation of tensile strength is much slower in the whole pulp reaction of peroxide with the fines on account of their larger specific surface area. After 120 minutes, the tensile strength of treated long fibres is comparable to that of whole pulp treated for 30 minutes.

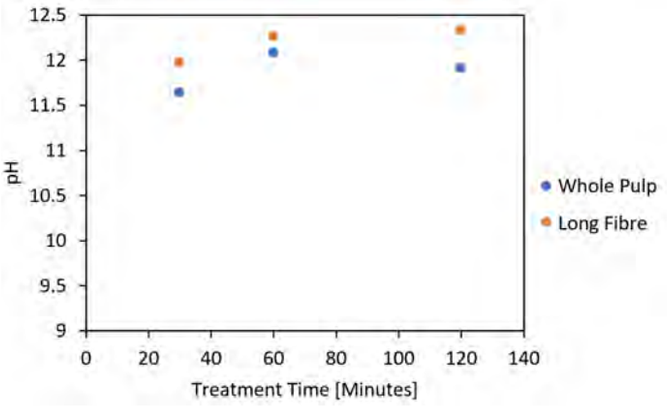

Figure 1. Final pH as a function of treatment time for whole pulp and long fibres.

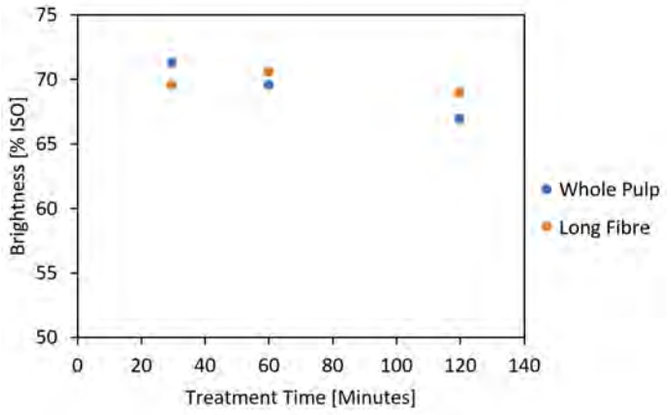

Figure 3. Brightness decreases over treatment time.

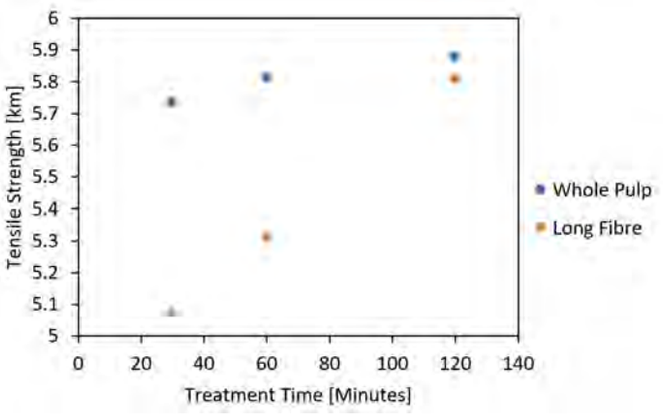

Figure 4. Tensile strength increases over treatment time.

PROJECT 1.3

After 30 minutes, the acid group content of whole pulp and long fibre is equivalent at 207 mmol/kg but the whole pulp has 13% greater tensile strength (Figure 5). Whole pulp tensile strength does not significantly increase as acid group content increases from 207 mmol/kg to 260 mmol/kg. A 0.6% increase in acid group content of long fibre results in a 4.7% increase in tensile strength. It is clear that tensile strength is not solely a function of acid group content; this agrees with our hypothesis that acid group distribution is also important to the development of tensile strength.

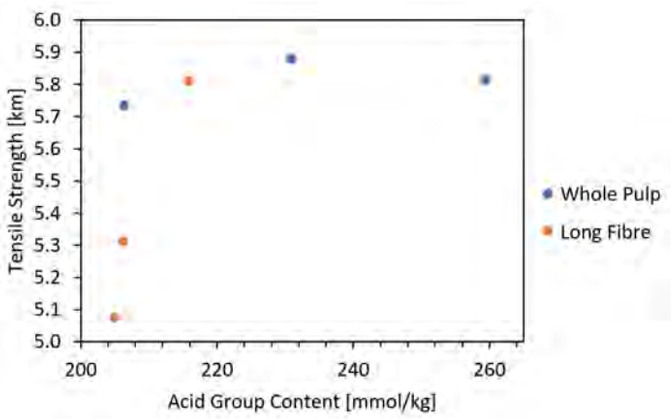

Figure 5. Correlating tensile strength with acid group content.

Conclusions

Whole pulp and long fibres respond differently to HAPT. Peroxide is consumed more rapidly by whole pulp but the final pH after HAPT of long fibres is greater. The brightness of the whole pulp decreases more rapidly in comparison to long fibres. Tensile strength and acid group content of whole pulp are developed within the first 30 minutes of HAPT. The tensile strength of long fibres develops slowly; as does acid group content. Differences in tensile strength of whole pulp and long fibres despite similar acid group content point to the role of fines and acid group distribution in paper strength.

Future Work

In future work, a detailed characterization of fines and fibres will be performed, prior to and post HAPT.

References

1. Beatson, R., Trajano, H., Mitra, S., K., and Maulit, C. (2021, November). ERMP November 2021 Newsletter. Energy Reduction in Mechanical Pulping. https://ermp.sites.olt.ubc.ca/files/2022/06/ERMP_Nov2021.pdf
2. Chang, X. F., Luukkonen, A., Olson, J., & Beatson, R. (2016). Pilot-scale investigation into the effects of alkaline peroxide pre-treatments on low-consistency refining of primary refined softwood TMP. Bioresources, 11(1), 2030-2042. https://doi.org/10.15376/biores.11.1.2030-2042
3. Dence, C., W., and Omori, S., (1996). Survey of hydrogen peroxide bleaching of mechanical and (chemi)mechanical pulp - factors affecting brightness. Pulp Bleaching: Principles and Practice: TAPPI 1996, pp. 457-489.
4. Maulit, C., Beatson, R., Trajano, H., Po, R., and Lai, R. (2022, November). ERMP November 2022 Newsletter. Energy Reduction in Mechanical Pulping.
5. Mitra, S., K., Maulit, C., Beatson, R., and Trajano, H. (2022, June). ERMP June 2022 Newsletter. Energy Reduction in Mechanical Pulping. https://ermp.sites.olt.ubc.ca/files/2023/01/ERMP_June2022.pdf
6. Moldenius, S., (1984). The Effects of Peroxide Bleaching on the Strength and Surface Properties of Mechanical Pulping. Journal of Pulp and Paper Science., vol. 10, pp. 172-177.
7. Noki, G., Beatson, R., Trajano, H., Maulit, C., Po, R., and Lai, R. (2023, November). ERMP November 2023 Newsletter. Energy Reduction in Mechanical Pulping.
8. Noki, G., Beatson, R., Trajano, H., Maulit, C., Po, R., and Lai, R. (2023, June). ERMP June 2023 Newsletter. Energy Reduction in Mechanical Pulping.

PROJECT 2.1

LIGNIN RICH FINES: SIMPLE ROUTES TOWARDS CREATION OF HYDROPHOBIC AND HYDROPHILIC FILLER ADDITIVES

Authors: Adam Wu and Scott Renneckar

Background

The subproject regarding the development of a fine-based hydrophobic filler for 3D printing of PLA has been completed, as our team member Siwei Chen has submitted her thesis. The research update was summarized in the previous report highlighting the impact of surface modification, fine loading, and physical treatments to modify the performance of the composite. Therefore, the current report will focus on the other subproject that aims to enhance the hydrophilicity of fines.

Previously, we reported on the direct esterification of softwood mechanical pulp fines using succinic anhydride, catalyzed by imidazole (referred to as SA modification) to produce hydrophilic fines as dry-strength additives for papers. The modification showed successful incorporation of carboxylic acid groups onto fines (near 0.5 mmol/g), resulting in enhanced hydrophilicity and intermolecular interactions between fine particles. When the fines were added to the long fibre fractions of thermomechanical pulp (TMP) as well as more refined bleached chemi-thermomechanical pulp (BCTMP), improvements in tensile and burst indices were observed to various degrees (up to 30%, as summarized in the previous report).

Results

The methodology we selected for the modification (direct esterification) of fines was based on a study that esterified pure cellulose pulp for cellulose nanofibrils (CNF) production (Beaumont et al., 2021). In order to obtain a deeper understanding of the esterification of the fines, considering that the fines contain > 40% lignin, we isolated the lignin from the starting and SA-modified fines for characterization. Lignin isolation was carried out by recovering "milled wood lignin" (MWL), which is known to preserve the native structure of lignin, by ball milling followed by extraction with the mixture of dioxane and water (96:4, v: v). Isolated lignin samples were subjected to gel permeation chromatography (GPC), differential scanning calorimetry (DSC), and nuclear magnetic resonance (NMR) analyses to determine the changes after SA modification on molecular weight and functional groups.

As Shown in Table 1, the lignin isolated from SA-modified fines had reduced molecular weight, potentially from the cleavage of β-O-4 linkages during the esterification process (40 °C, 6.25h) using succinic anhydride that resulted in a mild acidic environment. 31P NMR that quantified the hydroxyl groups of MWL indicated an increase in carboxylic acid by 0.15 mmol/g, which is direct evidence of the SA-esterification (Table 1, Figure 1). A decrease in aliphatic hydroxyl (OH) groups was also observed, likely due to the conversion of accessible OH groups into carboxylic acid (COOH) groups by esterification. The increase in the phenolic OH group was likely due to the cleavage of β-O-4 linkages, which was supported by a decrease in the molecular weight of lignin. The spectra of 13C NMR further indicated the increase in ester groups (as a result of esterification), as well as the reduction of primary and secondary OH groups (where the esterification occurred) in the lignin from SA-modified fines (Figure 1).

Table 1. Molecular weight, functional groups and glass transition temperature of mill wood lignin isolated from starting TMP fines and SA-modified fines, determined by GPC and NMR

Source of MWL	Mn (kDa)	Mw (kDa)	Aliphatic OH (mmol/g)	Phenolic OH (mmol/g)	Carboxylic acid (mmol/g)	Glass transition temperature (°C)
TMP fines	1.53	25.63	1.46	0.27	0.08	124.0
SA fines	0.68	6.44	0.95	0.53	0.23	59.4

PROJECT 2.1

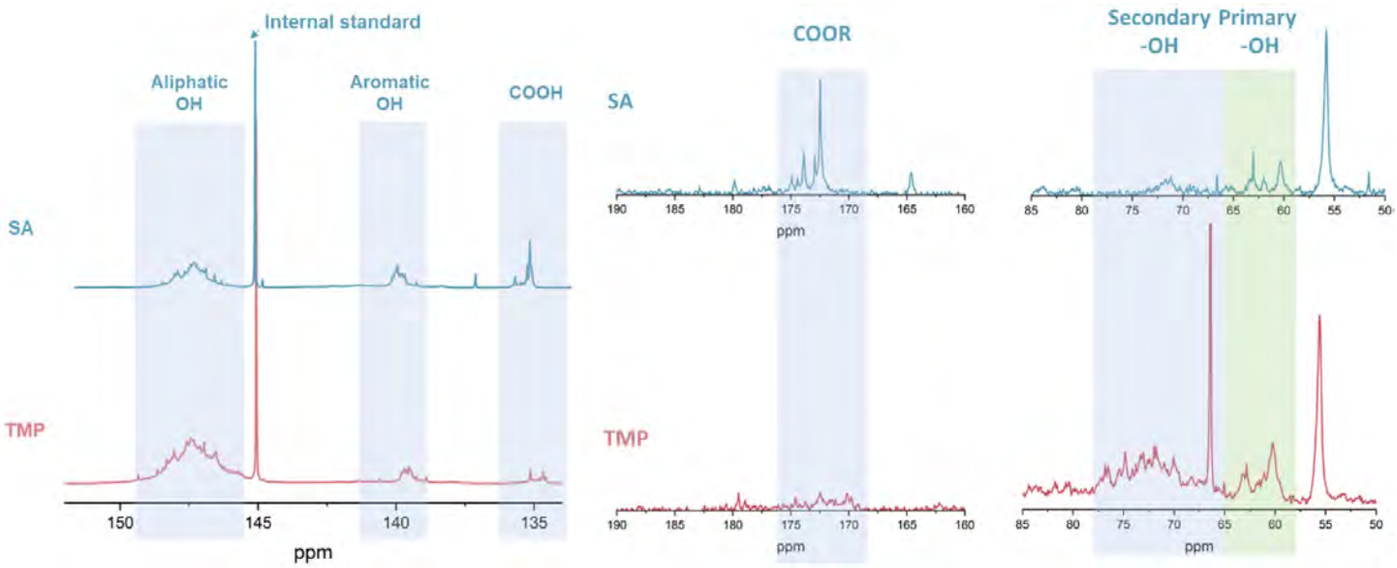

Figure 1.[31]P (left) and [13]C (right) NMR spectra of MWL isolated from TMP and SA fines

With the understanding that succinic anhydride and imidazole catalyzed the esterification of OH groups from the cellulose and lignin (and likely hemicellulose) components of fines, we then attempted to investigate the potential for producing fines-based functional materials. It was reported in our previous report that esterification resulted in around 0.5 mmol/g of carboxylic acid groups on the fines. This amount was comparable to the levels of acid groups reported in other studies that used esterification to produce cellulose nanofibrils (CNF) (Zheng et al., 2024). Therefore, we attempted to produce lignin-containing cellulose nanofibrils (LCNF) from modified fines through high-pressure homogenization using a microfluidizer (29000 psi for 2 passes at 1 wt.% consistency).

As shown in Figure 2, microfluidizer treatment resulted in a more uniform size distribution of particles with sizes smaller than 100 µm by removing the large particles with sizes greater than 300 µm. Since microfluidizers have been widely used for the production of nanocellulose, we then investigated whether this treatment resulted in lignin-containing cellulose nanofibrils (LCNF) from fines. The isolation of LCNF was carried out by centrifugation of the suspension at 3000g for 30 min, followed by the collection of the supernatant, based on the procedure described by Imani et al.(Imani et al., 2019). It was found that the LCNF content of microfluidizer-treated TMP and SA fines on a dry weight basis was 9.5% and 11.9%, respectively. The preliminary AFM images indicated that there were greater amounts of nanofibrils in the LCNF from SA fines, whereas the LCNF from TMP fines contained nanoparticles with a low aspect ratio (Figure 3). Additional analysis is underway to determine the cause of morphology, but several individual fibrils are visible in the image.

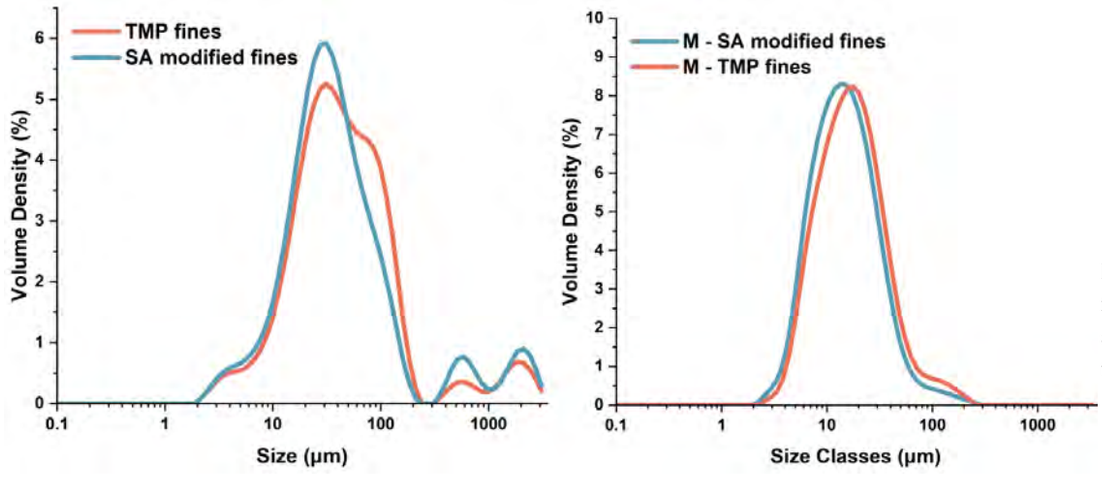

Figure 2. Size distribution of TMP fines and SA fines before (left) and after (right) microfluidizer treatment

PROJECT 2.1

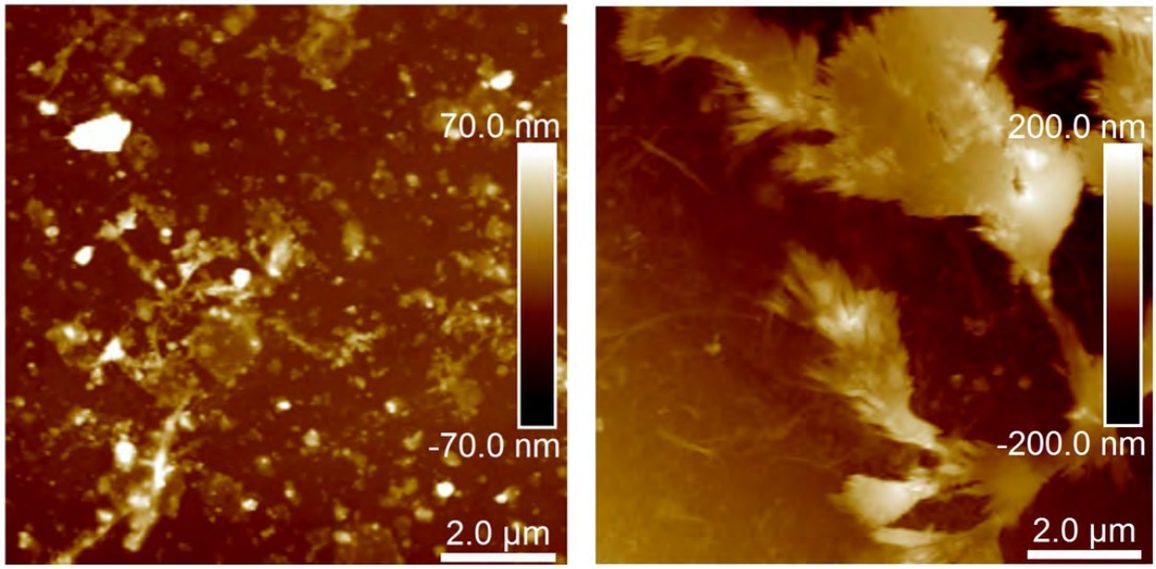

Figure 3. AFM images of LCNF isolated from microfluidizer-treated TMP (left) and SA (right) fines.

We subsequently tested the mechanical strength of the films derived from microfluidizer-treated TMP fines and SA-modified fines created through a simple filtration process. It was apparent that SA modification followed by homogenization resulted in particles that could form strong films with tensile strength greater than 40 MPa and Young's modulus exceeding 3000 MPa, significantly greater than those of the starting TMP fines. To further enhance the mechanical properties of the SA-fines-derived films, we employed cold pressing (room temperature and 20 MPa for 10 min) and hot pressing (140°C and 20 MPa for 10 min).

Cold pressing further increased the tensile strength to around 500 MPa, likely by physically enhancing the intermolecular bonding and densification of the material. In contrast, hot pressing involved a temperature much higher than the glass transition temperature of lignin (Table 1), leading to the relocation of lignin, which likely resulted in a more uniform distribution of lignin throughout the film. Consequently, hot pressing of SA fines-derived films resulted in the highest tensile strength (60 MPa) and Young's modulus (4500 MPa) (Figure 4).

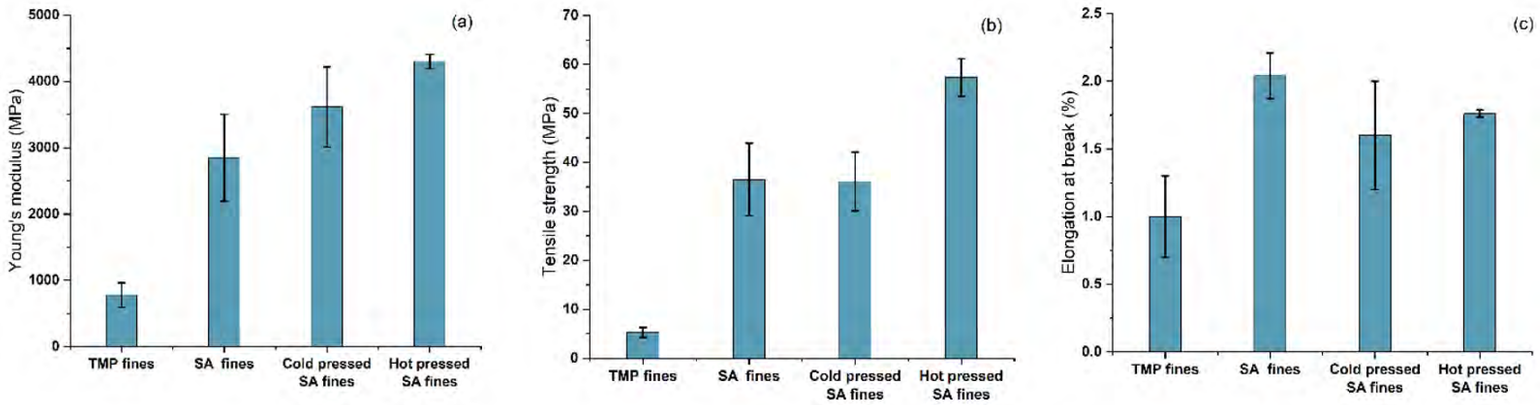

Figure 4. Mechanical properties of films derived from microfluidizer-treated fines.

PROJECT 2.1

Future Research

Future research will aim to further improve the mechanical strength of films by optimizing the hot-pressing temperature and increasing the content of LCNF present in the fines through tip sonication. Additionally, we will further characterize the films using microscopy techniques and test their functions, such as antioxidative and antimicrobial properties, provided by the 40% lignin contained in the fines, with the ultimate goal of producing advanced packaging materials from fines.

Acknowledgements

We would like to thank Mr. Ricky Hua (PhD candidate), Miss Nicole Ting and Miss Raewyn Rozak (undergraduate research assistants) for their contribution to the production and mechanical testing of the films.

References

1. Beaumont, M., Tardy, B.L., Reyes, G., Koso, T. V., Schaubmayr, E., Jusner, P., King, A.W.T., Dagastine, R.R., Potthast, A., Rojas, O.J., Rosenau, T., 2021. Assembling Native Elementary Cellulose Nanofibrils via a Reversible and Regioselective Surface Functionalization. J Am Chem Soc 143, 17040–17046. https://doi.org/10.1021/jacs.1c06502
2. Imani, M., Ghasemian, A., Dehghani-Firouzabadi, M.R., Afra, E., Borghei, M., Johansson, L.S., Gane, P.A.C., Rojas, O.J., 2019. Coupling Nanofibril Lateral Size and Residual Lignin to Tailor the Properties of Lignocellulose Films. Adv Mater Interfaces 6. https://doi.org/10.1002/admi.201900770
3. Zheng, D., Sun, X., Sun, H., Zhu, Y., Zhu, J., Zhu, P., Yu, Z., Ye, Y., Zhang, Y., Jiang, F., 2024. Effect of hornification on the isolation of anionic cellulose nanofibrils from Kraft pulp via maleic anhydride esterification. Carbohydr Polym 333, 121961. https://doi.org/10.1016/j.carbpol.2024.121961

PROJECT 2.2

FROM TREES TO TREATMENT: FUNCTIONALIZING TMP EXTRACTIVES

Authors: Yimin Wang, Cameron Zheng, Laurel Schafer, Heather Trajano

Background

Extractives such as terpenes and fatty/resin acids are potential sources of natural therapeutics.[1,2] Modification of the naturally complex structures may lead to novel or more potent therapeutics. One modification pathway is hydroaminoalkylation, the addition of an amine across a carbon-carbon double or olefinic bond; the Schafer group has developed a family of catalysts for such reactions.[3] In our earliest work, we demonstrated the addition of N-methylaniline (NMA) to limonene using our tantalum catalyst. This early work also considered combinations of other amines and terpenes. More recently, we have expanded this work to include decarboxylated fatty acids, such as linoleic acid (Fig. 1). Decarboxylation of linoleic acid allows access to a reactive α-olefin for amination by our catalyst.[4] Finally, computer modelling by the Page group (UBC Pharmaceutical Science), has shown that aminated terpenes have the potential to bind to and inhibit disease-relevant proteins of bacteria such as Mycobacterium tuberculosis.

The utilization of decarboxylated linoleic acid for hydroaminoalkylation was inspired by our previous investigation of extractives in pulp and mill process streams. Extraction of samples from Meadow Lake Pulp with organic solvent led to the detection of fatty and resin acids, specifically linoleic acid, abietic acid, and pimaric acid, through GC-MS (Fig. 2). We now aim to develop efficient and cost-effective methods to isolate wood extractives within pulp mill.

The foundational work of Kangas and Kleen[6] demonstrated the extractives content of fines is greater than that of long fibres. Bulk compositional analysis showed that fibrillar fines contained the greatest amount of extractives, followed by flake-like fines. The surface of both fibrillar fines and flake-like fines had a high surface coverage of extractives such as fatty acids. Kangas and Kleen proposed that ray cells are broken and release wood extractives into the process water during refining; the extractives are then re-adsorbed onto the surface of fines, especially fibrillar fines which have a higher specific surface area than fibres. Based on this previous work, we envision recovery of fines as a slipstream from the fibre line followed by recovery of extractives. This approach reduces flow rate and equipment sizing for extraction thus reducing cost. Analytical protocols for mill samples are under development. Once these protocols are established, we will investigate the desorption of extractives from fines.

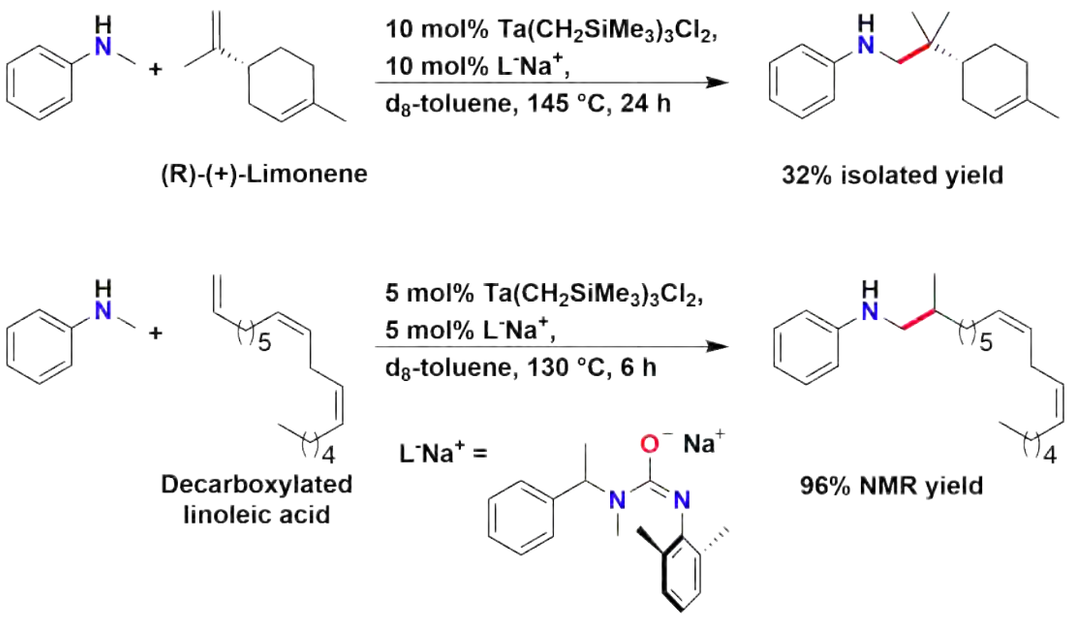

Figure 1. Reaction scheme for limonene and decarboxylated linoleic acid amination by hydroaminoalkylation.[5]

PROJECT 2.2

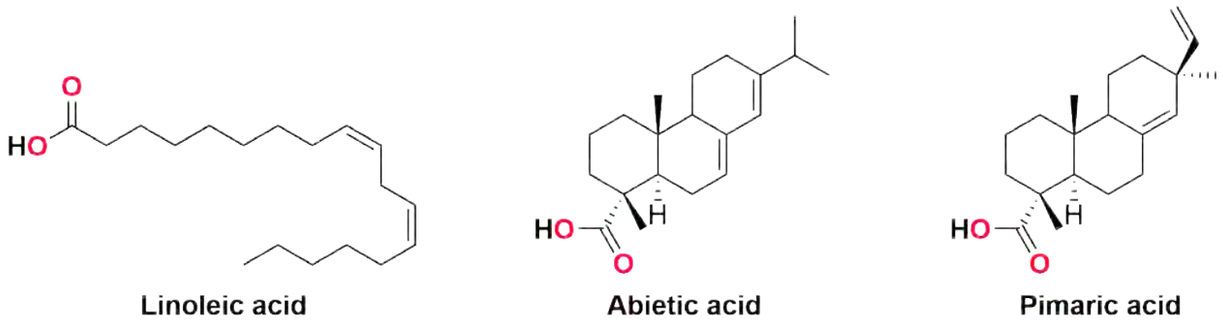

Figure 2. Turpentine amination with toluene as added solvent (A) and without added solvent (B). Product 1 is derived from β-pinene and product 2 is derived from limonene.

Methods

Process water and pulp samples were provided by Meadow Lake Mechanical Pulp. The samples were collected while the mill was conducting a softwood run (70% jack pine, 30% white spruce). They were clear white water (CWW, collected from disc filter downstream of refiners), interstage pressate (ISP, screw press before bleach plant), and pulp exiting interstage press (ISP pulp). In addition, Meadow Lake Pulp provided CWW concentrate and ISP concentrate. The concentrates were prepared using dewatering bags.

The fines recovery protocol is illustrated in Fig. 3. To recover fines from the CWW and ISP for compositional analysis, a 5 g O.D. process water sample was added to the Britt jar with a 200-mesh screen and filled up to 500 mL with distilled water. Long fibres have been retained for later analysis. The fines-ladden filtrate was centrifuged at 1,000 × g force. The supernatant was carefully recovered and a pellet of fines was collected for extraction with hexanes. The supernatant was subjected to a second centrifugation at 21,000 × g force in order to verify that 1,000 × g force was sufficient to recover all fines. Unavoidably, some supernatant remained with each pellet. Each fraction was subjected to hexane extraction. Due to the high solubility of linoleic acid in hexanes7, we anticipate complete recovery of extractives to the organic phase. Each pellet was suspended in 40 mL hexanes for 24 hours at 25°C. Liquid-liquid extraction was conducted with 40 mL of supernatant and 40 mL of hexanes at 25 °C for 1 hour. Separation of the aqueous and organic phases of the CWW samples was difficult due to the formation of a stable foam in the phase interface. The hexane extracts were dried in a rotary evaporator, subjected to trimethylsilyl (TMS) derivatization, and analyzed by gas chromatography-mass spectrometry (GC-MS). Hexadecane was used as an internal standard for GC-MS.

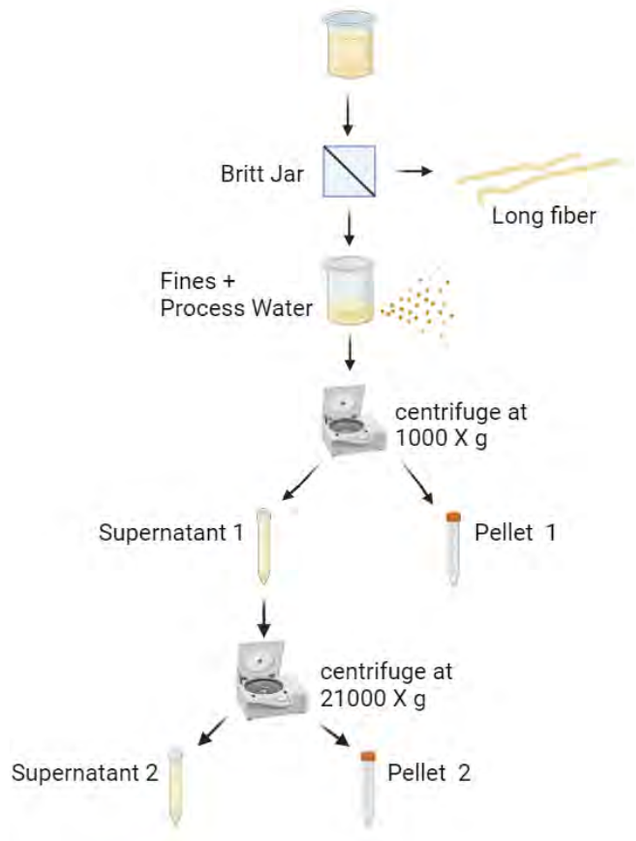

Figure 3. Flowchart of the wood fines separation procedure

PROJECT 2.2

Results

The composition and distribution of wood extractives in process water samples were investigated using GC-MS. Chromatograms of each sample are shown in Fig. 4. Relative area was calculated for peak compared to the total peak area in the chromatogram; only species with a relative area greater than 1% are reported. The CWW and ISP pellets collected after centrifugation at 1,000 × g force both contain abietic, dehydroabietic, isopimaric, pimaric, oleic, and linoleic acid, as shown in Table 1.

CWW and ISP supernatant samples contain the same fatty acids as the pellets, plus oxodehydroabietic acid (Table 1). The presence of oxodehydroabietic acid in the supernatant may indicate that oxodehydroabietic acid has a greater affinity for the aqueous phase than the surface of fines. All detected fatty acids have been previously identified as extractives of White Spruce and Jack Pine. However, as achieving complete separation between pellet and supernatant after centrifugation was difficult, some extractives detected in the pellet may be due to the residual supernatant. The extracts of CWW and ISP supernatants have a higher concentration of extractives than the corresponding fines, as evidenced by a greater peak area (Figure 4).

Table 1. Extractives identified using a GC-MS library search. The italicized extractives are the 2 most concentrated within a sample. of aminated β-pinenes first reported in DiPucchio et al., 2019 and selected for in silico modeling.

CWW Pellet 1	CWW Supernatant 1	ISP Pellet 1	ISP Supernatant 1
Abietic acid	Abietic acid	*Abietic acid*	Abietic acid
Dehydroabietic acid	*Dehydroabietic acid*	*Dehydroabietic acid*	*Dehydroabietic acid*
Isopimaric acid	Isopimaric acid	Isopimaric acid	Isopimaric acid
Pimaric acid	*Pimaric acid*	Pimaric acid	*Pimaric acid*
Oleic acid	Oleic acid	Oleic acid	Oleic acid
Linoleic acid	Linoleic acid	Linoleic acid	Linoleic acid
	Oxodehydroabietic acid		Oxodehydroabietic acid

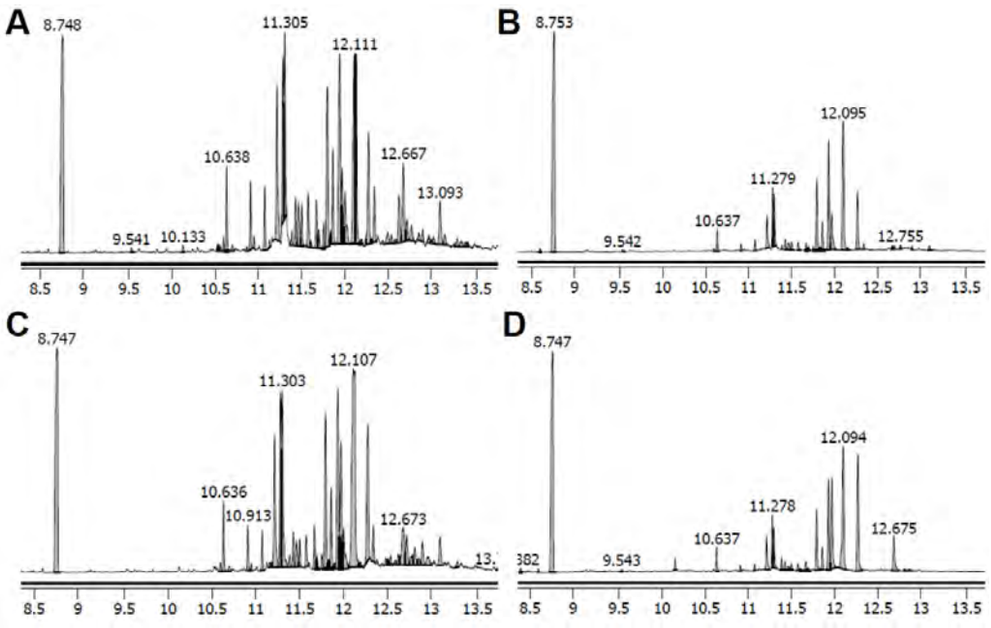

Figure 4. CWW supernatant (A) and ISP supernatant (C) contain a greater number of extractives with greater peak areas than CWW pellet (B) and ISP pellet (D), respectively. Hexadecane, the internal standard, appears at a retention time of ~8.748 minutes.

PROJECT 2.2

Results

GC-MS analysis of CWW Pellet 2 detected only trace amounts of fatty acids indicating that 1000 × g force is sufficient to pellet the majority of fines (Figure 5). The fatty acid composition and concentration of CWW Supernatant 2 was similar to CWW Supernatant 1. Supernatant 1 provides a representative analysis of the process water fraction and Pellet 1 contains all wood fines, including fibrillar and flake-like fines. The ISP pulp was disintegrated and then subjected to the same fines separation, hexane extraction, and GC-MS protocols. Fatty acid identification in the ISP pulp and its long fibre fraction will be included in the slides presented at the steering committee meeting.

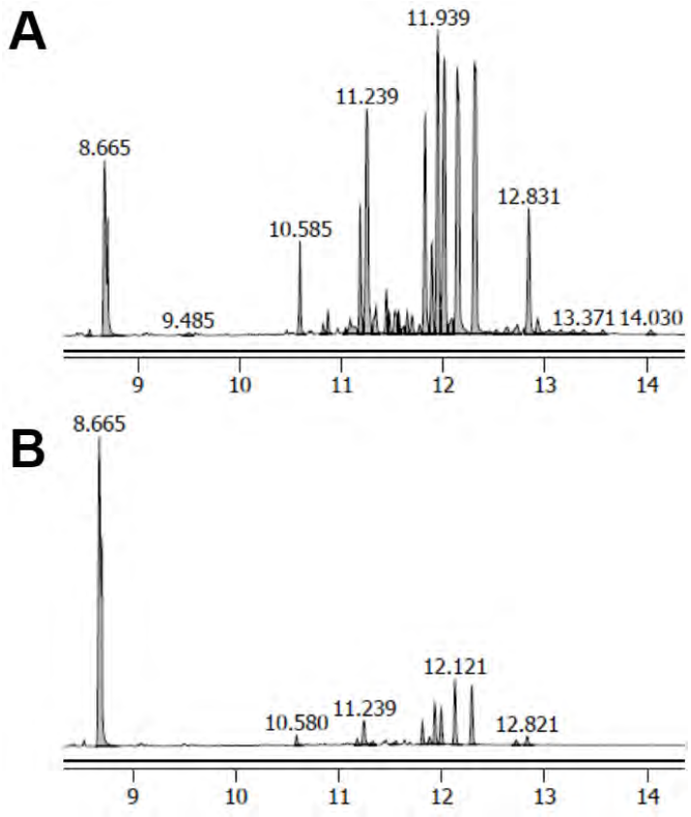

Figure 5. CWW pellet 1 (A) contains a greater number of extractives with greater peak areas than CWW pellet 2 (B). Hexadecane, the internal standard, appears at a retention time of 8.665 minutes. The hexadecane peak in pellet 2 appears larger because the y-axis is normalized to the tallest peak.

Conclusions & Future Research

The Britt jar followed by centrifugation at 1000 × g force enabled the recovery of fines from process water. Fatty acids were detected in the process water and fines. A greater number and concentration of extractives were present in the aqueous phase than in the fines. A second centrifugation at 21,000 × g force produced a pellet containing very little extractives.

The developed analytical protocol will be applied to the CWW and ISP concentrates to evaluate the impact of dewatering on extractives content. The protocol will be further refined to enable full quantification.

Ultimately, the isolation of fatty acids from pulp mill streams should be done without organic solvent. Desorption of extractives from fines will be attempted by varying suspension temperature, pH, and ionic strength. Hexane extraction followed by TMS derivatization and GC-MS analysis will be used to evaluate the effectiveness of desorption.

References

1. Cox-Georgian, D.; Ramadoss, N.; Dona, C.; Basu, C. Med. Plants From Farm to Pharm. 2019, 333–359.
2. Desbois, A. P. Recent Patents on Anti-Infective Drug Discovery, 2012, 7, 111-122.
3. DiPucchio, R. C.; Rosca, S.-C.; Schafer, L. L. J. Am. Chem. Soc. 2022, 144, 11459–11481.
4. Liu, Y.; Kim, K. E.; Herbert, M. B.; Fedorov, A.; Grubbs, R. H.; Stoltz, B. M. Adv. Synth. Catal. 2014, 356, 130–136.
5. DiPucchio, R. C.; Rosca, S.; Athavan, G.; Schafer, L. L. ChemCatChem 2019, 11, 3871–3876.
6. Kangas, H.; Kleen, M. Nordic Pulp & Paper Research Journal. 2004, 19(2), 191-199.
7. C. W. Hoerr; H. J. Jarwood, J. Phys. Chem. 1952, 56, 9, 1068–1073

PROJECT 2.3

PRODUCTION, CHARACTERIZATION, AND APPLICATIONS OF MFLC DERIVED FROM MECHANICAL PULP FINES

Authors: Mariana Frias de Albuquerque, James Olson, Boris Stoeber, Heather Trajano

Background

This project aims to reduce the energy required to produce microfibrillated lignocellulose (MFLC) from mechanical pulp fines for various paper applications through the implementation of enzymatic hydrolysis prior to refining.

In a previous phase of this project, we investigated the production of MFC using short fibres obtained from softwood bleached chemi-thermomechanical pulp (BCTMP). The pulp was fractionated using a 0.8 mm hole screen and then refined at the UBC Pulp and Paper Centre pilot plant. The refined short fibres were subsequently combined with long fibres, and paper handsheets were created for mechanical testing. The refined short fibres contributed to the tensile strength of the paper, while the long fibres contributed to the bulk (Seifert et al., 2023). The specific refining energy correlated well with the elasticity of fibre suspensions through rheological properties. Furthermore, we investigated the effect of enzymatic hydrolysis of short BCTMP fibres before refining using the PFI mill. We evaluated the effect of pH and hydrolysis incubation temperature on post-refining fibre morphology and inter-fibre interactions. It was found that when pulp was incubated at a higher temperature, its structure became softer and more prone to fibrillation. Additionally, when incubation pH was made more alkaline, it modified the fibre surface charge and allowed enzymes to break down the microfibrillar structure of the cell walls without removing fibrils from the fibre surface.

At our last committee meeting, we presented the influence of enzymatic hydrolysis duration and enzyme dosage, on the morphology of short fibres post-refining. We have determined a trade-off between incubation time and enzyme dosage for fibre length and fibrillation targets. Longer exposure of fibres to cellulases, about 2 hours, would allow the process to incorporate dosages as low as 0.1 wt.%. Since then, we have investigated the effect of low-dosage endoglucanase on the refining of non-fractionated BCTMP to assess enzyme action on a broader range of fibre lengths. The results of this study are briefly discussed in this document.

Results

This section presents the results and discusses their implications in the context of the research objectives. To emulate low-consistency refining conditions, BCTMP at 3.5 wt.% consistency was hydrolyzed with 0.1 wt.% endoglucanase for 2 hours in a shaking incubator at pH 5 and 60 °C, agitating at 180 rpm. Hydrolyzed fibres were subjected to increasing PFI refining from 0 to 5,000 revolutions. A control group was incubated and refined at the same conditions without the addition of the enzyme for comparison purposes. Fibre morphology was evaluated using an L&W FiberTester+. The quality of the fibres was evaluated through the Canadian Standard Freenes (CSF) and the quantification of fines using a Dynamic Drainage Jar (DDJ).

The following analysis examines our findings and their significance. The results in Figures 1-3 present fibre properties relative to the initial properties of untreated, unrefined BCTMP fibres shown in Table 1.

Fibre length is a useful metric for assessing the degree of pulp refining and paper qualities. Previous research has shown that fibre length decreases as the refining level increases (Kerekes, 2005). Figure 1-a shows how the relative length-weighted average length of BCTMP is affected by enzymatic hydrolysis and increasing PFI refining energy, here expressed in the number of revolutions.

Table 1. Experimental matrix to assess the effect of incubation time and enzyme dosage on fibre morphology.

Property	*Value*
Length-weighted fibre length	1.46±0.02 mm
Fibril area	4.60±0.06 (%)
Fibril perimeter	19.2±0.05 (%)
Kink index	1.02±0.05
Slender fines content	53.1±0.2 (%)
Coarser fines content	11.0±0.1 (%)
DDJ fines content	13±3 (%)
CSF	583±3 ml

PROJECT 2.3

Due to the low intensity of the PFI mill, there was no significant reduction in length with the increase in refining. The addition of an enzymatic hydrolysis step did not cause an additional decrease in fibre length, contrary to previous observations in softwood kraft pulp. The accessibility of enzymes to cellulose was possibly limited by the high lignin content present (approximately 22 wt.%), in addition to the fact that in mechanical pulp, lignin covered approximately 60% of the fibre surface area (Kleen et al., 2003). Consequently, the accessible area for enzymes is significantly reduced for this substrate.

Although there was no significant reduction in fibre length, the enzyme-hydrolyzed fibres had a higher kink index than non-hydrolyzed fibres (Figure 1-b). The kink index is associated with the number of abrupt bends along the length of the fibres (Page et al., 1985). Even without enzyme treatment, the kink index increases with PFI revolutions due to the number of impacts of the refining bars on the fibres. The kink index of unrefined, hydrolyzed fibres is 10% greater than untreated, unrefined fibres. The kink intensifies with refining energy, reaching a 50% increase compared to untreated, unrefined fibres. The internal glycosidic bonds in cellulose chains cleaved by endoglucanase create points on the fibre surfaces that are susceptible to bending and kinking.

The external fibrillation of the fibres is measured by the L&W+ in two distinct ways: fibril area, which is associated with the extent of peeling, and fibril perimeter, which is associated with the quantity of fibrils attached to the fibres. Figure 2 depicts the change in relative fibril area (a) and fibril perimeter (b) with PFI refining and enzymatic hydrolysis.

First, for untreated fibres, both the fibril area and fibril perimeter increase with PFI revolutions. Due to the impact of the metal bar on the fibres and the shear between fibres during refining, the surface of the fibres peels off. This outer surface is likely part of the middle lamella or primary cell wall. After enzymatic hydrolysis, the fibres lose approximately 5% of their external fibrillation. The fibrils' surface is readily accessible for enzyme binding (Hildén et al., 2005). Interestingly, the percentage increase in fibrillation of fibres hydrolyzed and refined at 1,000 PFI revolutions is more significant than that of untreated fibres, indicating that there was a softening of the surface of the fibres during enzymatic hydrolysis. The variation of the fibril perimeter with refining from 0 to 1,000 revolutions is more pronounced than that of the fibril area for the same refining range; the hydrolyzed fibres were more susceptible to abrasion forces, increasing the amount of fibril bundles attached to the central axis rather than increasing the fibril area.

When PFI revolutions are increased from 3,000 to 5,000, the fibril area of hydrolyzed and non-hydrolyzed fibres both increased by 10%. The change in fibril perimeter of hydrolyzed and non-hydrolyzed fibres from 3,000 PFI revolutions to 5,000 revolutions was also equivalent. These observations reinforce the hypothesis that the enzymatic action was limited to the surface of the fibres. The initial refining (1,000 revolutions) imposed the energy necessary to peel the hydrolyzed regions of the fibres. At higher levels, the refining energy was applied to newly exposed surfaces which had not undergone enzymatic hydrolysis.

The reduction in fibrillation during hydrolysis may have increased the fines fraction. Figure 3 shows the evolution in the fines content with PFI refining and enzymatic hydrolysis. The L&W + distinguishes fibres from fines according to the ISO standard, in which any element with a length smaller than 0.2 mm is considered a fine. Furthermore, the equipment characterizes the fines as coarser or slender (Figure 3-a).

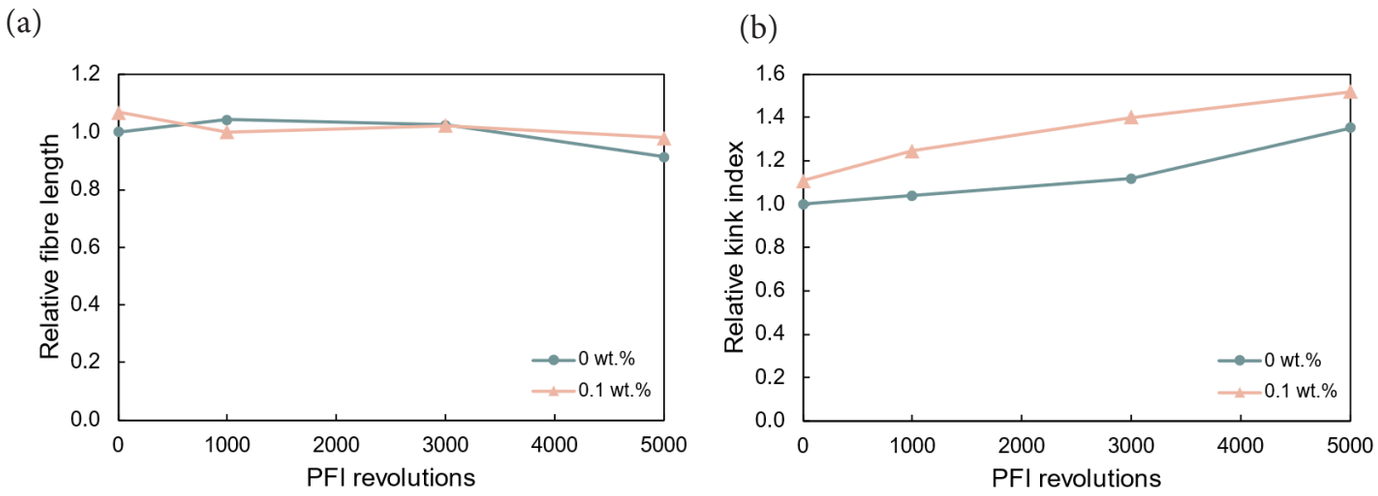

Figure 1. Relative length-weighted fibre length (a) and relative kink index (b) of PFI-refined BCTMP fibres incubated with 0 wt.% and 0.1 wt.% endoglucanase.

PROJECT 2.3

Coarser and slender fines' content are associated with particulate and slim fines, based on a combination of the width and length of the fine particles. The internal method with which the equipment distinguishes the classes of fines is proprietary to the instrument supplier (Hyll, 2016). After hydrolysis and 1,000 PFI revolutions, the slender fines fraction increased slightly (less than 5%) due to the enzymatic action that partially plucked the fibrils from the surface of the fibres. From 3,000 revolutions onwards, the development of the slender fines from hydrolyzed fibres is like that of untreated fibres.

In contrast, the coarser fines fraction (approximately 7%) is lost during enzymatic hydrolysis, which suggests that the enzymes hydrolyzed this type of fine. This fines' fraction increases slightly after being refined for 1,000 PFI revolutions. As seen previously, further development of this fraction matches that of untreated fibres. Figure 3-b shows the development of the weight-based fines fraction obtained by DDJ. Initially, there was no difference in the fines fraction after hydrolysis, which is different from the results from the fibre tester. As the L&W+ characterizes fibres through microscopic imaging, it can identify fines that make a negligible contribution to the mass of the pulp suspension. At 1,000 revolutions and 3,000 revolutions, the fines measured by DDJ may be too small to be detected by the fibre tester (4 µm resolution).

Figure 4 presents microscopy images of the fines collected with the drainage jar from unrefined, untreated and hydrolyzed pulp. The solids from untreated fibres comprise very short fibres (around 0.1 mm in length), fragments (less than 0.1 mm in length), and fibrils. The fines from treated fibres appear hydrolyzed, corroborating the findings on coarser fines. The figure shows patterns of degradation promoted by endoglucanase previously seen in the literature (Vanderghem et al., 2012) and research from the Pulp and Paper Center at the University of British Columbia. Future analysis of quantification of soluble sugars will help clarify the extent of hydrolysis of fibrils and coarser fines, and the creation of fines.

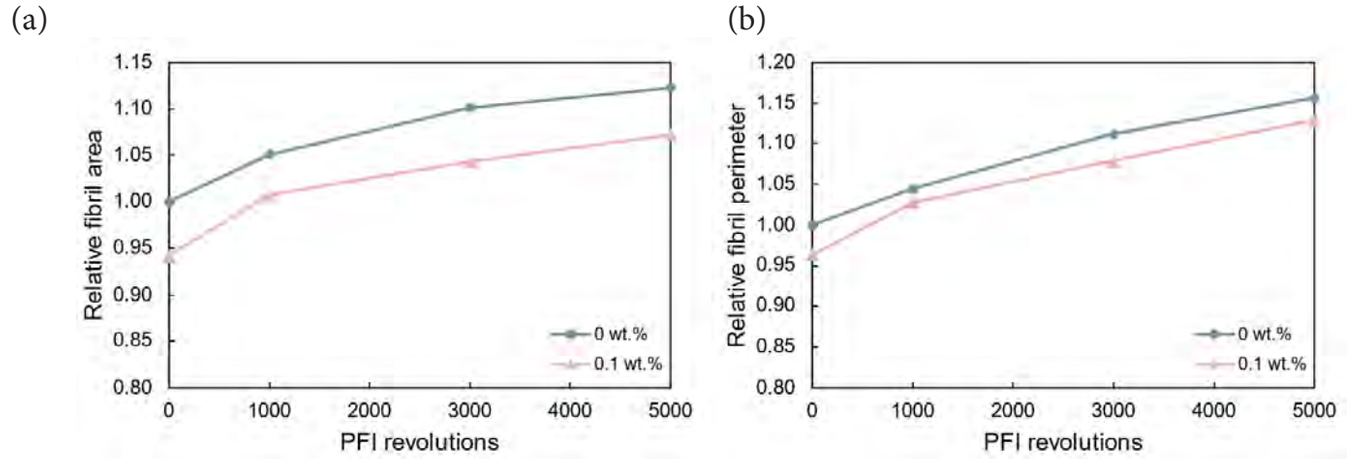

Figure 2. Relative fibril area (a) and relative fibril perimeter (b) of PFI-refined BCTMP fibres incubated with 0 wt.% and 0.1 wt.% endoglucanase.

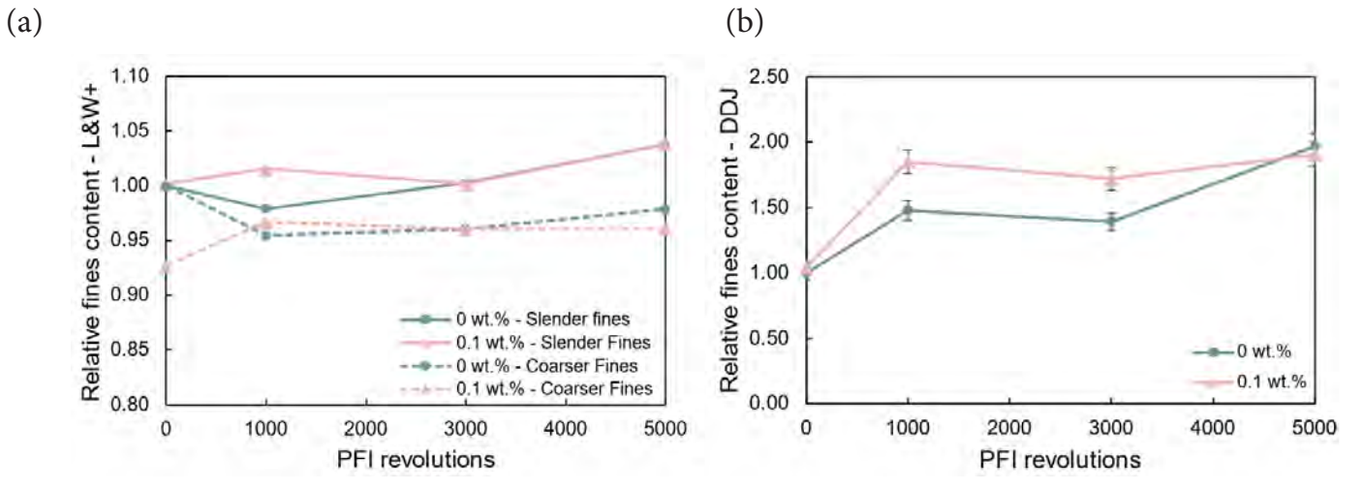

Figure 3. Fines content of PFI-refined BCTMP fibres incubated with 0 wt.% and 0.1 wt.% endoglucanases as obtained from a) L&W+ with a distinction between slender and coarser fines, and b) 200-mesh screen via DDJ.

PROJECT 2.3

Finally, treated and untreated fibres had the same fines content when refined at 5,000 revolutions. Between 3,000 and 5,000 revolutions, there is a generation of fines from fracture of fibres. Simultaneously, the very short fibres and fines continue to fracture, creating fines. As the refining intensity of the PFI mill is very low, it was not possible to notice an increase in the fines fraction for hydrolyzed fibres after refining at 5,000 revolutions.

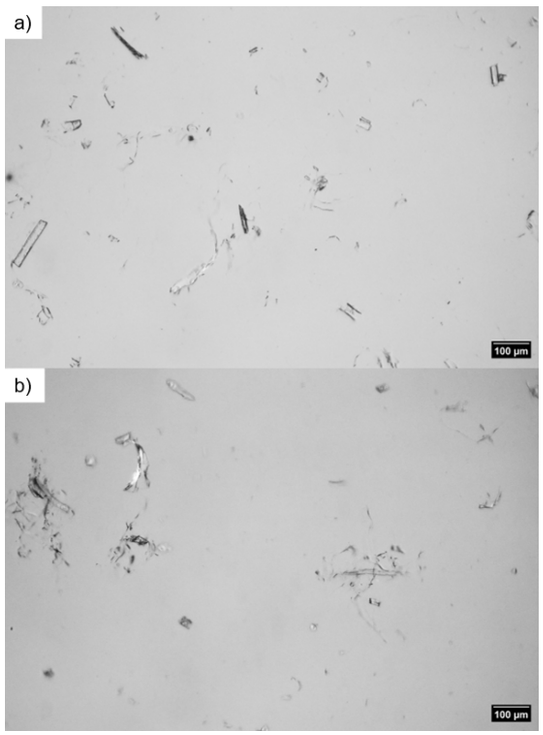

Figure 4. Optical microscopy analysis of unrefined BCTMP fines separated using a 200-mesh screen via DDJ. Panel a) presents fines obtained from untreated fibres, and panel b) presents fines from pulp hydrolyzed with 0.1 wt.% endoglucanase.

Enzymatic hydrolysis of BCTMP was limited, with little change in morphological development throughout the refining process. However, the modification of external fibrillation and the generation of fines may have modified the quality of the pulp, such as freeness. Figure 5 shows the development of CSF. CSF of non-hydrolyzed pulp decreases with increasing refining levels. A parallel can be drawn between the development of the fines fraction characterized by DDJ and the development of freeness with refining. Thus, it is possible to conclude that the presence of fines was the factor with the greatest impact on the drainability of the fibres. The reduced freeness and greater proportion of slender fines in hydrolyzed BCTMP refined to 1,000 revolutions may result in paper with greater tensile strength. Future handsheet testing is planned for confirmation.

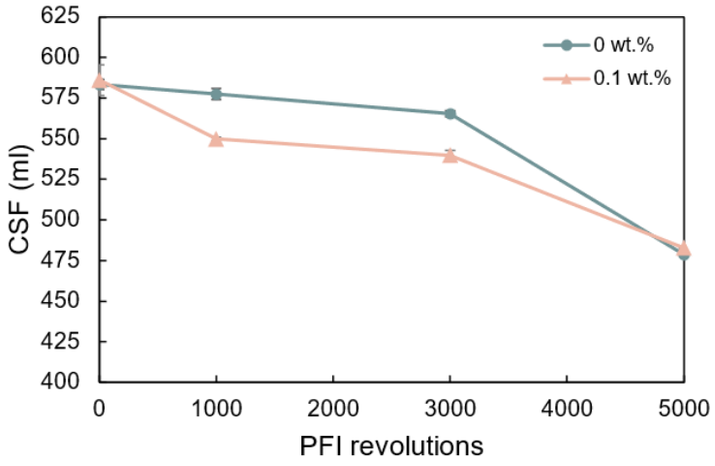

Figure 5. CSF of PFI-refined BCTMP fibres incubated with 0 wt.% and 0.1 wt.% endoglucanase.

Future Research

We will investigate the effect of hemicellulases, such as mannanase and xylanase, on fibre properties. We will also evaluate the role of preexisting mechanical pulp fines in modifying fibre morphology by including a fines separation step (DDJ) before enzymatic hydrolysis. Additionally, we will assess the incorporation of a highly alkaline treatment before enzymatic hydrolysis as an attempt to increase fibre porosity and, hence, enzyme accessibility to the fibre cell wall.

Finally, once laboratory-scale tests are completed, we will move on to larger-scale trials using the UBC Pulp and Paper Centre pilot plant's single disc refiner. In these trials, the refining action will be more representative of a mechanical pulping mill, and we can quantify potential energy savings from enzyme hydrolysis.

PROJECT 2.3B

INCORPORATING MICROFIBRILLATED CELLULOSE FOR HIGH STRENGTH AND HIGH BULK

Authors: Fariba Yeganeh, Michael Bilek, James Olson

Background

Continuining our exploration of new applications for mechanical pulps through combining fractionation and LC refining. In this study, our aim is to showcase the utilization of LC refining in the production of MFLC, while also creating high bulk sheets as an experimental platform for comprehending MFLC composites. The reinforcement capability of the aspen- MFLC was examined by blending it with BCTMP- spruce- pine- fir (SPF) whole fibers and BCTMP- SPF long fiber fractions at various mass ratios. Our primary objective was to develop a method for the production of high bulk sheets with strengthened mechanical and physical properties for packaging applications. We also aimed to establish a cost-effective and environmentally sustainable approach for reinforcing sheets without significantly increasing energy usage during the LC refining process.

Methods

LC Refining Trials

Two LC refining trials were conducted employing Aikawa-16" single disc refiner, one using BCTMP- SPF to produce the LC-refined sheets, and another using BCTMP- aspen to produce MFLC. LC refining was operated in a continuous recirculating loop employing specific fine bar plates, at a flow rate of 250 L/min, and 1200 rpm. Both trials were aimed to attain the maximum cumulative specific refining energy (SRE). For producing MFLC, BCTMP- aspen was LC refined a high SRE of close to 1600 kWh/t to effectively break down aspen fibers into fine micro-sized particles. For LC- refined sheets preparation, a plate with the BEL of 2.74 km/rev was applied which enabled continuous circulating refining of BCTMP-SPF up to 545 kWh/t. 6 samples were collected during the trial at different SREs with about 100 kWh/t interval.

Handsheets Composites preparation

Two types of composite handsheets were prepared by blending MFLC with SPF fibers; one involved a blend of 0 to 20% MFLC with SPF whole fibers, and the other utilized by blending 0 to 20% MFLC with SPF long fibers, aimed for high bulk sheets preparation. To achieve long fibers, SPF fibers were fractionated using a Bauer-McNett classifier, and long fibers (R14, R 28, and R48 fractions) were collected.

The handsheets were prepared utilizing a mechanical handsheet maker, fitted with a recirculation loop to retain MFLC into the sheets structure according to TAPPI T205 om-88. The produced sheets were tested according TAPPI 402 sp-13. All sheets were characterized for bulk, tensile strength and tear strength.

Results

Tensile strength

An increase in SRE demonstrated a positive impact on both the tensile index and tensile energy absorption (TEA) of the resulting sheets, Figure 1a and 1b. The highest tensile index and TEA were observed for the sheet formed of highly LC refined pulp at 545kWt/t. Increasing SRE develops the tensile index and TEA by beating fibers and broke fiber down in fines (Seifert et al. 2023). Although, highly LC- refined pulp led to higher tensile strength, it resulted in low bulk and also an excessive energy was consumed during re-pulping.

The incorporation of MFLC into both the whole fibers and long fiber fractions resulted in an improvement in the tensile strength of the produced composites. Long fibers that mainly contribute to bulk development, led to high bulk composite sheets while the composites produced from whole fiber plus MFLC displayed higher tensile index and TEA. This can be attributed to the influence of fins on tensile index development, alongside the enhanced fiber-fiber binding by MFLC (Brodin and Eriksen 2015). The tensile index depends on the bonding capability of fibers, flexible fibers facilitate substantial contact areas conducive to fiber-to-fiber bonding (Dutt et al. 2009; Jahan and Rawshan 2009). In the composites whole fibers plus MFLC, the preservation of fines, along with the reinforcement of the fiber network by MFLC, enables the fibers to withstand higher stress levels, resulting in increased the tensile index and TEA. Tensile strength stands out as a key mechanical parameter to consider for sustainable packaging applications. Throughout transportation and distribution, packaging materials must withstand heavy loads. Hence, materials with good tensile strength are particularly valuable for packaging applications (Jayakumar et al. 2019).

PROJECT 2.3B

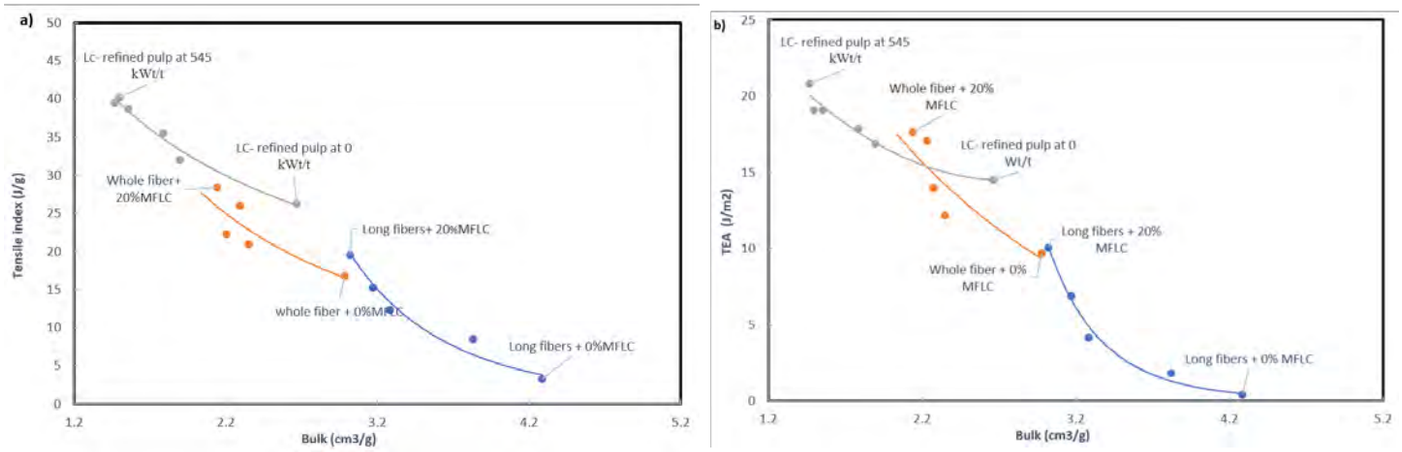

Figure 1. Relationship between a) tensile index and bulk b) TEA and bulk. Legend: LC refined pulp: LC- refined SPF BCTMP in grey. Whole fiber+ MFLC in orange and long fibers + MFLC in blue.

Tear strength

Figure 2 show a decrease in tear index of the LC- refined sheets when SRE increased from 0 to 545 kWt/t. One drawback of LC refining is the occurrence of fiber shortening, leading to a subsequent decrease in tear index, particularly noticeable at higher refining intensities (Luukkonen et al. 2010; Elahimehr et al. 2015).

The addition of MFLC to high bulk fibers (long fibers) significantly increased the tear index of the produced composites. But MFLC addition to the whole fibers, did not notably reinforce the tear strength of the resulting composites, Figure 5a and 5b. However, the composites formed of whole fiber plus MFLC exhibited a higher tear index compared to the those made of long fibers plus MFLC. In the long fiber plus MFLC composites, replacing the long fibers with heavily refined MFLC reduced overall fiber length but enhanced fiber network and superior bonding. This indicates the positive impact of bond strength and fiber network on tear index in addition to fiber length. The preservation of fiber length alongside the addition of MFLC enhanced inter-fiber bonding, increasing the tear strength. In the whole fiber plus MFLC composites which contained short fibers and fines as well, it is likely that the composites reached maximum tear resistance, and the additional MFLC did not contribute to further improvement. In the comparison between the composite sheets and the LC – refined sheets at an equivalent SRE, composite sheets showed higher tear index and bulk, Figure 4a and 4b. The addition of MFLC contributed to enhanced tear strength without significantly reducing bulk. These findings underscore that MFLC addition not only improves tear strength of the composites but also helps reduce energy required to produce high-strength sheets.

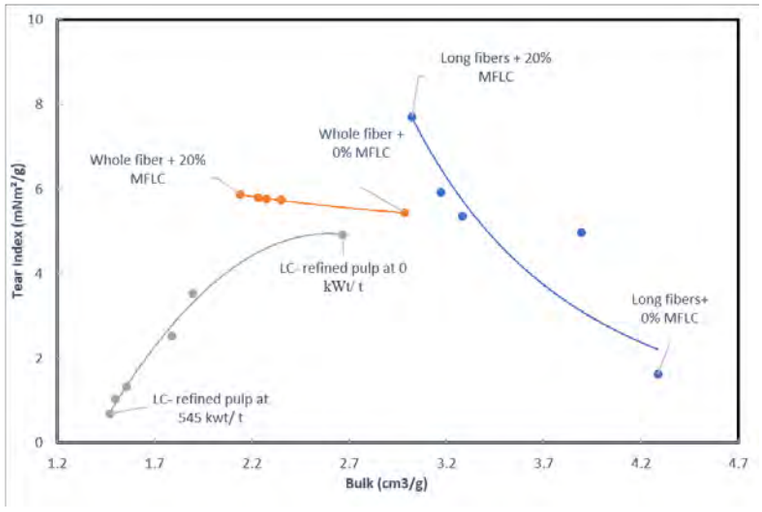

Figure 2. Relationship between tear index and bulk. Legend: LC refined pulp: LC- refined SPF BCTMP in grey. Whole fiber+ MFLC in orange and long fibers + MFLC in blue.

PROJECT 2.3B

Conclusions

This study investigated the preparation of high-bulk, strengthened composite sheets tailored for packaging applications by integrating MFLC into SPF whole pulp and fractionated SPF long fibers. We conducted a comparative analysis of the properties of the composite sheets with the sheets produced from LC-refined pulp. The results demonstrated increasing refining energy during LC refining resulted in denser structures and high tensile strength. However, LC refining caused fiber shortening and reduced bulk and tear strength. In addition, substituting SPF fibers with MFLC in the composite sheets improved tear resistance by improving bonding network between fibers and maintaining the stiff long fiber component. Composite sheets exhibited higher tear strength and bulk, indicating their potential suitability for packaging applications. Although the LC- refined sheets exhibited higher tensile strength, their denser nature may potentially limit their suitability for packaging applications. These findings underscore the advantages of incorporating MFLC into SPF fibers to enhance specific properties relevant to packaging requirements.

Future Work

In future work, a detailed characterization of MFLC will be performed. We will continue our investigation on MFLC based films for packaging applications.

References

1. Brodin FW, Eriksen Ø (2015) Preparation of individualised lignocellulose microfibrils based on thermomechanical pulp and their effect on paper properties. Nordic Pulp & Paper Research Journal 30:443–451
2. Dutt D, Upadhyay J, Singh B, Tyagi C (2009) Studies on Hibiscus cannabinus and Hibiscus sabdariffa as an alternative pulp blend for softwood: An optimization of kraft delignification process. Industrial crops and products 29:16–26
3. Elahimehr A, Olson JA, Martinez DM (2015) Low consistency refining of mechanical pulp: how plate pattern and refiner operating conditions change the final properties of pulp. Nordic Pulp & Paper Research Journal 30:609–616
4. Hildén, L., Väljamäe, P., & Johansson, G. (2005). Surface character of pulp fibres studied using endoglucanases. Journal of Biotechnology, 118(4), 386–397.
5. Hyll, K. (2016). Image-based quantitative infrared analysis and microparticle characterisation for pulp and paper applications. KTH Royal Institute of Technology.
6. Jahan MS, Rawshan S (2009) Reinforcing potential of Jute pulp with TREMA ORIENTALIS (NALITA) pulp. BioResources 4:921–931
7. Jayakumar A, Heera K, Sumi T, et al (2019) Starch-PVA composite films with zinc-oxide nanoparticles and phytochemicals as intelligent pH sensing wraps for food packaging application. International Journal of Biological Macromolecules 136:395–403
8. Kerekes, R. J. (2005). Characterizing refining action in PFI mills. Tappi J, 4(3), 9–14.
9. Kleen, M., Kangas, H., & Laine, C. (2003). Chemical characterization of mechanical pulp fines and fiber surface layers. Nordic Pulp & Paper Research Journal, 18(4), 361–368.
10. Luukkonen A, Olson J, Martinez D (2010) Low consistency refining of mechanical pulp, effect of gap, speed and power. Journal of Pulp and paper Science 36:28–34
11. Page, D. H., Seth, R. S., Jordan, B. D., & Barbe, M. C. (1985). Curl, Crimps, Kinks and Microcompressions in Pulp Fibres – Their Origin, Measurement, and Significance. In V. Punton (Ed.), Trans. Of the VIIIth Fund. Res. Symp. Oxford, 1985 (pp. 183–227). Fundamental Research Committee (FRC), Manchester.
12. Seifert, R., Gharehkhani, S., Vargas Figueroa, D., Mercuur, J., & Olson, J. (2023). Engineering the paper production by combined fiber fractionation and reinforcement with microfibrillated cellulose. Cellulose, 30(5), 3201–3217.

PROJECT 3.1

CHEMICAL MODIFICATION AND ADVANCED CHARACTERIZATION OF FIBRES

Authors: Kudzanai Nyamayaro, Sam N. M. Brown, Emily Cranston, Mark Martinez

Background

In this project, our aim is to modulate the bulk and tensile properties of pulp fibres through chemical modification and to characterize these modifications by developing methodologies to study water absorption in paper. Section 1 describes the use of hydroxypropyl methylcellulose (HPMC) to simultaneously increase the bulk and tensile properties of bleached chemical thermo-mechanical pulp (BCTMP). Section 2 covers the use of confocal microscopy to track water movement in paper, which can be applied to visualize additives and provide insights into the chemical modification of pulp.

Results

Section 1: The chemical and mechanical modification of pulp fibres is a potential route to increase the bulk of paper without reducing the mechanical properties. Project 3.1. aims to apply a chemical modification to obtain low-density paper (i.e., high bulk) while maintaining favourable mechanical properties using BCTMP. Currently, we have demonstrated that HPMC, a low-cost and renewably sourced cellulose derivative, can be applied as a surface modifier for mechanical pulps to simultaneously enhance bulk and tensile properties of paper. HPMC adsorbs onto the fibre surface, increasing fibre-fibre interactions through polymer entanglement which increases the tensile properties Additionally, HPMC increases bulk by preventing fibre collapse during drying. Since the last newsletter, we have aimed to answer several questions about the effective use of HPMC. First, can lower amounts of HPMC be used? Second, can different types of HPMC be just as effective? Lastly, will the adsorption of HPMC be affected by the refining process? If so, this would dictate whether HPMC should be applied to the pulp itself or onto preformed paper, as we have shown that both are similarly effective (in the absence of other paper additives and intense mechanical processing).

In this work, BCTMP handsheets were prepared using a pre-treatment method that involves adding HPMC into the pulp slurry prior to papermaking. High molecular weight (K100M) and lower molecular weight (K99) HPMC were used to investigate the influence of HPMC molecular size on the bulk and tensile properties (Figure 1a-b). The bulk and tensile properties were retained or improved for both K100M and K99. A greater increase in tensile index was observed for lower molecular weight K99-HPMC compared to higher molecular weight K100M-HPMC. The improvement was attributed to improved solubility of lower molecular weight HPMC, leading to higher adsorption of HPMC onto the pulp. HPMC loading was reduced to 0.25 wt% to investigate the influence of concentration. The lower loading was sufficient to improve the properties of BCTMP, highlighting that lower quantities of HPMC can be used to improve bulk and tensile properties.

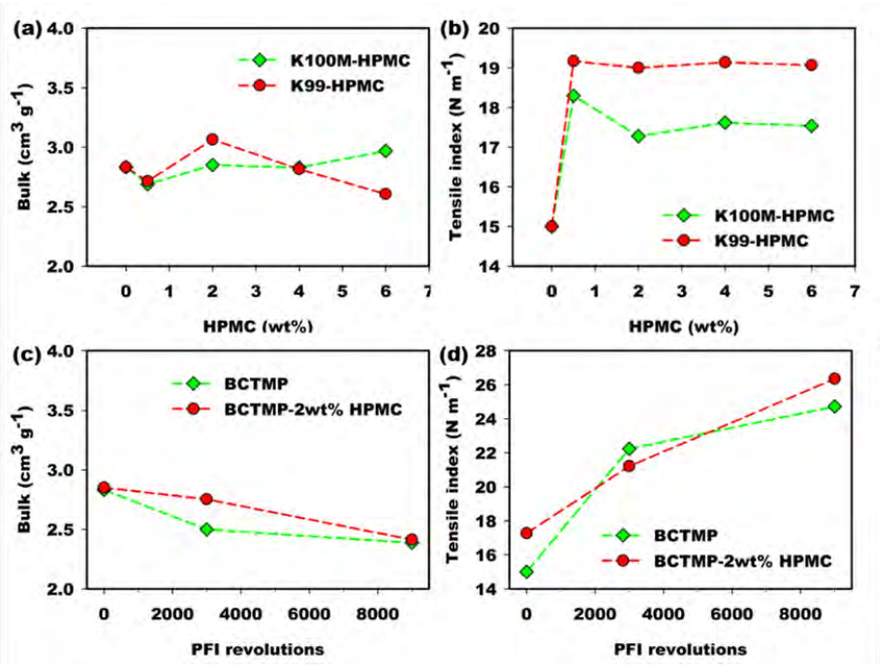

Figure 1. (a) Bulk and (b) tensile index of handsheets pre-treated with high molecular weight K100M-HPMC and low molecular weight K99-HMPC. Both bulk and tensile properties were enhanced by HPMC under all tested conditions. (c) Bulk and (d) tensile index of PFI refined BCTMP and BCTMP pretreated with 2 wt.% of high molecular weight K100M-HPMC. The advantageous increase in properties is retained after refining, demonstrating irreversible binding of HPMC to BCTMP.

PROJECT 3.1

The robustness of HPMC adsorption on the pulp was tested using PFI refining (Figure 1c-d). The bulk and tensile properties were retained or improved when the pulp with 2 wt.% HPMC was refined at 3000 and 9000 revolutions. In summary, the effectiveness and robustness of using HPMC to enhance the properties of mechanical pulp has been demonstrated. This is shown by preserving the improved properties with lower HPMC loadings, using HPMC with different structures, and through the refining process.

Section 2: Promoting or impeding water absorbency, a critical material property in paper-based products, relies on accurately characterizing absorption behaviours. However, these phenomena are currently lacking scientific consensus, especially at the microscale. In particular, it has been noted that classical models for imbibition in porous media, such as the Bell-Cameron-Lucas-Washburn (BCLW) equation can be inaccurate, and we theorize that such models do not encompass all the physical mechanisms necessary to characterize absorption in paper. Significantly, the BCLW equation predicts that liquid should travel quickest in the larger (30 µm) external pores of the paper. However, the findings of our previous study1 suggest that liquid travels in the smaller internal pores of the paper, consisting of the fibre lumen (10 – 20 µm) and intra-fibre pores in the fibre wall (20 nm). Since the previous newsletter, where we detailed the initial phase of a systematic study into liquid absorption in paper, we have continued to develop new measurement methodologies and have generated some interesting results. Based on our observations, we posit that certain microscale imbibition behaviours have significant effects on water absorption in paper at the macroscale and should be accounted for in new models for absorption.

Shown in Figure 2 is X-ray radiography of the wetting process and confocal laser scanning microscope imaging of water movement in the external and internal pores of a blotter paper sample. In Figure 2a, the presence of partial saturation is visually observed in the sheet, as measured by X-ray radiography. The top dark blue portion corresponds to low moisture content, where the sheet is dry. Directly below is a teal-coloured region, where the paper has a medium saturation level of ~0.5. Next is a region transitioning from pale yellow colours to bright yellow, representing a further increase in saturation of 0.7 - 1.0. In total, the X-ray radiography data demonstrates that a saturation gradient is present in the paper during wicking. This is an important finding since one of the assumptions of the BCLW model is complete saturation behind the wetting front. Confocal microscopy was used to further examine the reasons for this effect at the microscale. In Figure 2b, the internal pores (i.e., fibres, in blue) can be seen filling before the external pores (in green) which are only partially saturated in the second frame. In the third frame, the internal pores have a similar appearance compared to the second frame, while the external pores display significant filling. Finally, by using a higher magnification (Figure 2c), we observed that the leading edge of the wetting front consists of liquid in the internal pores only, confirming the results of our previous study using iron tracers[1]. In summary, the wetting mechanism of paper was studied using X-ray radiography and the path of water movement through the macro and micro pores of the paper was visualized using confocal microscopy.

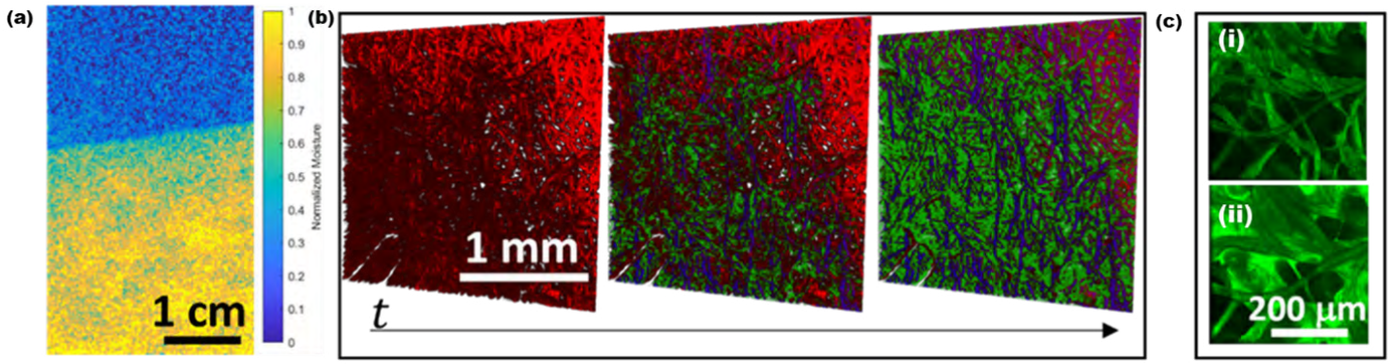

Figure 2. Overview of experimental results for the control sample. (a) An example radiograph of the control sample, showing gradient saturation of a handsheet in contact with water at the bottom. (b) Representative frames of a dual-staining timelapse for the control sample, with the background image in red, liquid in the internal pores in blue, and liquid in the external pores in green. (c) Example frames of absorption for the control sample at higher magnification, showing green liquid in the internal pores (i) prior to filling the external pores (ii).

PROJECT 3.1

To demonstrate the possible application of this confocal microscopy visualization method, the staining protocol shown in Figure 2b was applied to track water movement in chemically modified BCTMP handsheets and furthermore, to assess whether the chemical modification was located in/on the fibres. More specifically, we looked at (1) BCTMP with adsorbed HPMC, which is slightly more hydrophobic than unmodified fibres (following the work in Section 1 and Figure 1) and (2) hydrophobically-modified BCTMP (process: tannic acid adsorption followed by Schiff base reaction with the hydrophobic molecule butyl amine, i.e., BCTMP-Butylamine). In the unmodified BCTMP (Figure 3a), the internal pores (blue) and the external pores (green) were saturated with liquid. Conversely, in the hydrophobic BCTMP-Butylamine (Figure 3b) the internal pores (blue) are saturated, while very little liquid is in the external pores (green). This indicates that the hydrophobic modification is primarily distributed on the external surface of the fibre that forms the external pores. In addition to being able to determine the site of chemical modification, the technique could be used to visualize the presence of HPMC on the surface of handsheets. Figure 3c shows a snapshot of a staining experiment for an HPMC-treated BCTMP handsheet. Here, a single staining liquid is used, and the liquid is shown in green regardless of the pore system. The presence of pooling liquid (Figure 3c red arrow) was observed and was attributed to HPMC polymer chains that form coiled aggregates that hold a lot of water when they are not fully dissolved (i.e., HPMC microgels) and appear to cluster on the surface of the paper.

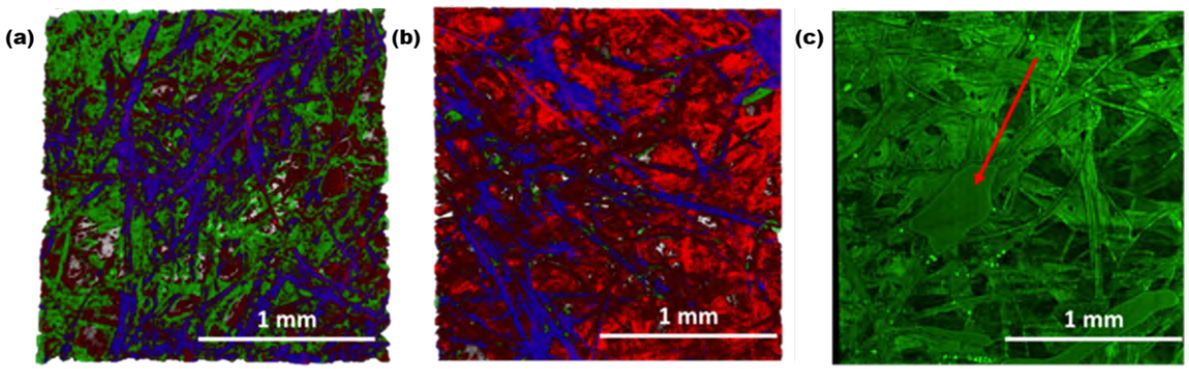

Figure 3. Confocal microscopy images of (a) BCTMP and (b) hydrophobic BCTMP-Butylamine handsheets highlighting the presence of liquid in the external pores (green) and internal pores (blue). The absence of liquid in the external pores for BCTMP-Butylamine indicates that the hydrophobic modification is confined to the external pores, i.e., the outside of the fibres. (c) BCTMP modified with HPMC. The red arrow points at HPMC microgels (i.e., polymer aggregates that hold water) on the surface of the paper.

Future Research

Section 1: In the future, the efficiency of HPMC binding to BCTMP in the presence of other additives used in papermaking will be investigated. This will show how well HPMC is compatible with typical additives. Additionally, the best way to add HPMC during pulping/processing/papermaking will be further studied, for example, should the addition be during high or low consistency refining. Also, various commercial HPMC polymers of different sizes and functionalities will be explored to find the most suitable option (along with a rough cost analysis).

Section 2: To continue investigating the physical mechanisms responsible for these behaviours, we conducted similar experiments on papers with physical and chemical alterations: paper treated with alkyl ketene dimer (AKD) blocking the external pores, compressed paper with reduced external pore sizes, and humidified paper with swollen fibres. These altered samples illustrate that interphase mass transfer and swelling are also important mechanisms to account for when modelling absorption. Further details will be discussed in upcoming journal publications.

References

1. E.S. Ferreira, J. Drummond, A. T. V. Veiga, A. Sibellas, S. Brown, E. D. Cranston, and D. M. Martinez, 2023. “Mapping absorbency in cellulosic fibres with iron tracers”. Carbohydrate Polymers, 311, 120785.

PROJECT 3.2

ADVANCED CHARACTERIZATION - X-RAY COMPUTED TOMOGRAPHY

Authors: Anderson Veiga, Lewis Mason, James Drummond, André Phillion,Emily Cranston, Mark Martinez

Background

X-ray Computed Tomography has the potential to offer detailed insight into the internal 3D structure and fibre network of pulp fibres and paper products in a non-destructive manner.[1]

For paper and cellulose-based materials, X-ray computed tomography enables visualization of fibre distribution, voids, and fibre morphology.[2] However, challenges arise when trying to distinguish the distribution of blended pulp fibres or the structure of a specific fibre morphology due to their chemical similarity. In such cases, labelling or staining with elements possessing different X-ray attenuation coefficients becomes necessary.[3] The approach of labelling to enhance contrast using X-ray computed tomography is commonly employed in clinical applications4 to increase the absorption coefficient, and can similarly be extended to pulp fibers. The X-ray absorption coefficient, μ, is given by:

$$\mu = \frac{\rho Z^4}{AE^3} \quad (1)$$

where ρ is the density, Z is the atomic number, A is the atomic mass, and E is the X-ray energy. From Eq. (1), materials possessing higher density and higher atomic number are strong candidates to enhance X-ray absorption as labelling agents. Iron oxide nanoparticles have been explored for visualizing the distribution of small fractions of pulp and nanocellulose fibrils in paper[3], due to the enhanced density of iron oxide (5.2 g/cm^3 for magnetite, Fe_3O_4) and the higher atomic number associated with iron (Z = 26). As a comparison, the density of pulp fibres is 1.5 g/cm^3, while the atomic number of carbon is Z = 6.

In previous reports, we detailed the development of imaging protocols using X-ray computed tomography for wood chips and BCTMP handsheets, alongside an image processing toolbox that allowed the characterization of wood chips, fibre, and sheets. We are now expanding the use of X-ray computed tomography to visualize different length fractions and different types of pulp through labelling, enabling the identification of specific morphology and pulp types.

Results

Structure Visualization: We have developed a protocol to enhance the visualization of the internal structures of handsheets by labelling the phase of interest with iron oxide nanoparticles. The iron-labelling protocol involved in-situ synthesis and deposition of the nanoparticles onto the surface of long fibres (Figure 1a). Multi-cycle deposition was conducted to achieve an iron loading of 16% w/w after the fourth cycle, resulting in enhanced contrast when visualized by X-ray computed tomography. Figure 1 shows an example of X-ray computed tomography results. In this figure, we layered unlabelled fibres over top of iron-labelled fibres in a syringe (Figure 1a) and compared the scan and segmentation results for fibres scanned in air (Figure 1b), as well as fibres, scanned immersed in oil (Figure 1c). Beginning with Figure 1b, it can be seen that enhanced contrast from the deposition of nanoparticles allowed for segmentation using an integer threshold, although the complete and accurate segmentation to visualize entire fibres was not possible. Thus, we immersed the fibres in hydrocarbon oil with a density of 0.9 g/cm^3, close to the density of unlabelled pulp fibres (1.5 g/cm^3), and re-scanned the sample via X-ray computed tomography.

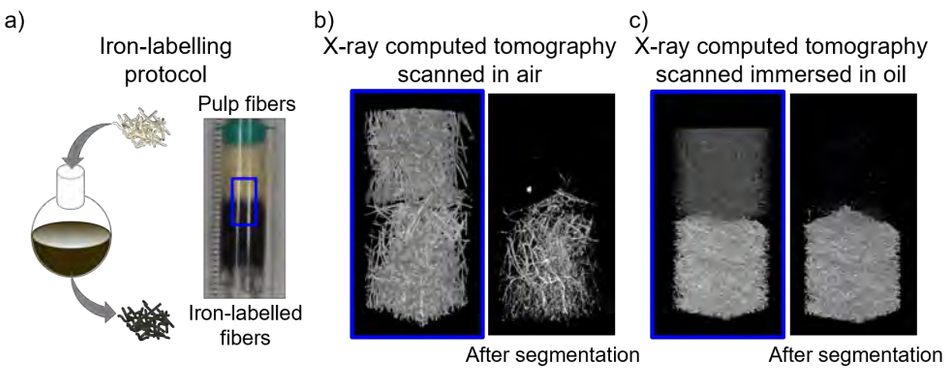

Figure 1. (a) Iron oxide nanoparticle-labelling protocol and fibres inside a syringe, with the blue area representing the scanned region; (b) X-ray computed tomography image of fibres scanned in air and the result after segmentation showing iron-labelled fibres; (c) X-ray computed tomography image of fibres scanned when immersed in oil and the result after segmentation showing iron-labelled fibres.

PROJECT 3.2

Thus, we immersed the fibres in hydrocarbon oil with a density of 0.9 g/cm³, close to the density of unlabelled pulp fibres (1.5 g/cm³), and re-scanned the sample via X-ray computed tomography. This strategy was employed to match the X-ray absorption of the background signal and unlabelled fibres and enhance the visualization of the iron-labelled fibres. The result, shown in Figure 1c, provided for optimal imaging conditions. From this work, we can conclude that the best results using integer threshold for segmentation of paper handsheets are achieved by combining iron oxide nanoparticles as labelling agents with oil immersion. This image-processing algorithm is simple and requires minimal expertise.

We incorporated the iron-labelled fibres into different handsheets to visualize the distribution of fibres at 2% w/w. As can be seen in Figure 2, it was very difficult to separate the iron-labelled and unlabelled fibres when the X-ray computed tomography dataset was acquired in air (Figure 2b, d, f), but the separation was very good when the X-ray computed tomography dataset was acquired in oil (Figure 2c, e, g), allowing for segmentation of the iron-labelled fibres (Figure 2f). This result demonstrates the potential to investigate the distribution of long fibres in handsheets and enables future studies correlating structure and paper performance.

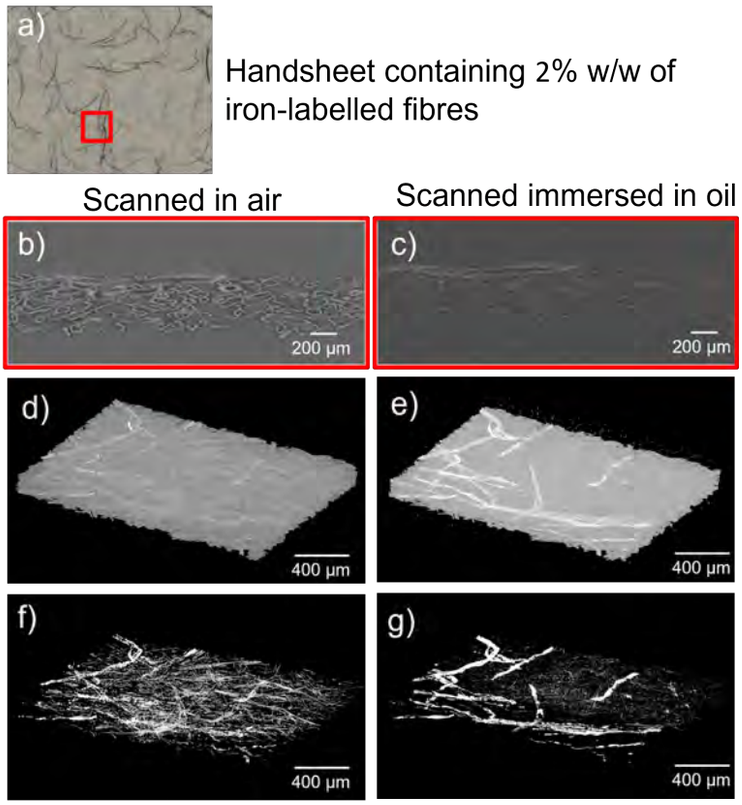

Figure 2. (a) Micrograph of a handsheet containing 2% w/w of iron-labelled fibres, with a red area representing the scanned region; Cross-sections, 3D rendering, and segmentation of X-ray computed tomography image for handsheets scanned in (b, d, f) air and (c, e, g) immersed in oil.

Machine Learning Image Segmentation: While the oil immersion method is novel, helpful and straightforward to improve segmentation of the iron-labelled fibres, it may not always be possible to implement based on the imaging/sample setup. Further, as the fibres become saturated in oil, they are no longer suitable for analysis. As such, to avoid immersing the fibres in oil, we developed an advanced image processing algorithm based on machine learning using a convolutional neural network. To train the network we provided it with two X-ray computed tomography datasets, the first a scan of normal fibre and the second a scan of iron oxide labelled fibre. Figure 3 shows the resulting segmentation for handsheets containing 0.1% w/w and 2% w/w iron-labelled fibres. As can be seen, after training, the neural network clearly segments the fibre distributions even at very low loadings of iron-labelled fibres. The neural network was able to classify the fibres into two groups: iron-labelled fibres and unlabelled fibres.

Future Research

Our next steps include optimizing the iron-labelling protocol to propose a faster and more efficient method for depositing iron-oxide nanoparticles as labelling agents to enhance the contrast for X-ray computed tomography. We will also apply and adjust this protocol to various pulp types and morphologies, assisting the development of other projects in the ERMP. This optimized iron-labelling protocol combined with the advanced segmentation algorithm has the potential to provide visual insights into the rule of mixture for pulps, visualize the distribution and retention of fines during drainage and wet pressing, and expand the development of pulp-based products (i.e. pulp foams) by the identification of different size fractions and types and correlate their role on the structure.

PROJECT 3.2

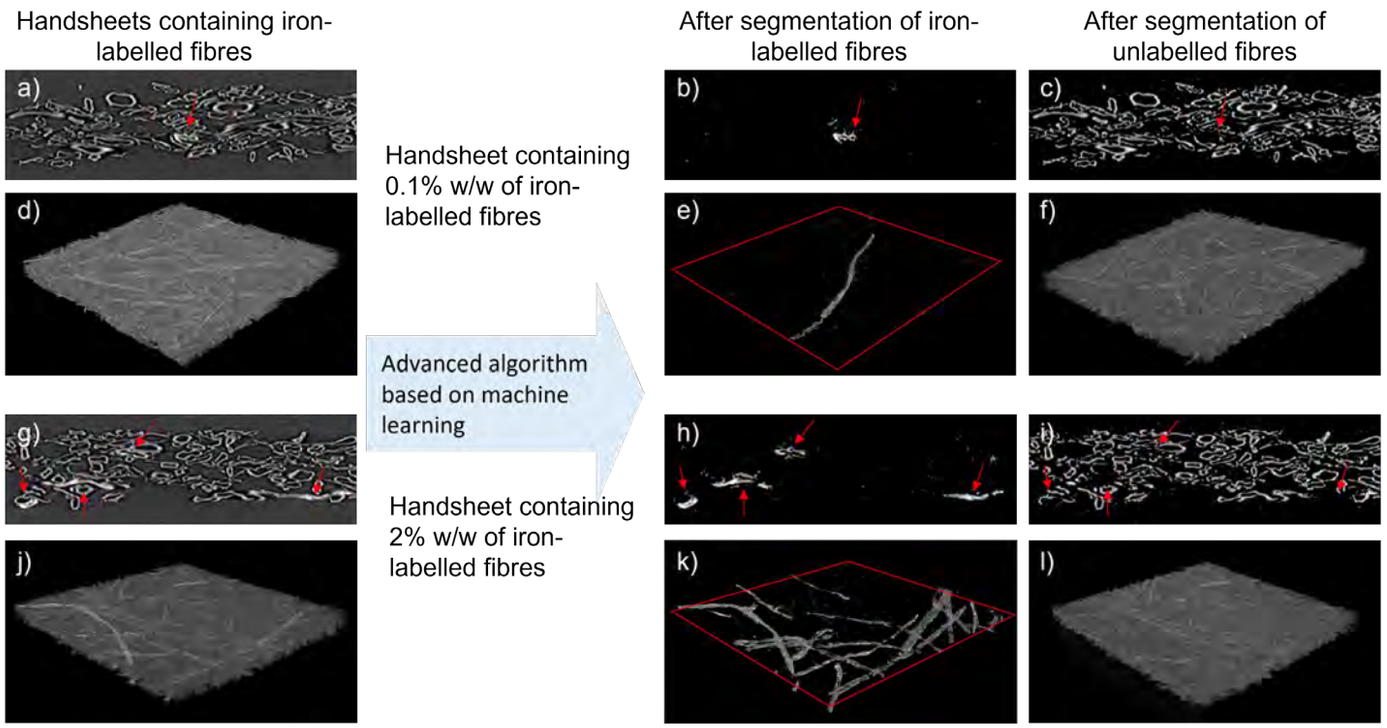

Figure 3. (a, g) Cross-section and (d, j) 3D rendering of X-ray computed tomography dataset for a handsheet containing 0.1% and 2% w/w of iron-labelled fibres. Images (b, e, and h, k) show segmentation of the iron-labelled fibres while (c, f, and i, l) show the unlabelled fibres

References

1. Wernersson, E. L. G.; Borgefors, G.; Borodulina, S.; Kulachenko, A. Characterisations of Fibre Networks in Paper Using Micro Computed Tomography Images. Nordic Pulp & Paper Research Journal 2014, 29 (3), 468–475. https://doi.org/10.3183/npprj-2014-29-03-p468-475.
2. Marulier, C.; Dumont, P. J. J.; Orgéas, L.; Rolland Du Roscoat, S.; Caillerie, D. 3D Analysis of Paper Microstructures at the Scale of Fibres and Bonds. Cellulose 2015, 22 (3), 1517–1539. https://doi.org/10.1007/s10570-015-0610-6.
3. Hobisch, M. A.; Zabler, S.; Bardet, S. M.; Zankel, A.; Nypelö, T.; Eckhart, R.; Bauer, W.; Spirk, S. How Cellulose Nanofibrils and Cellulose Microparticles Impact Paper Strength—A Visualization Approach. Carbohydrate Polymers 2021, 254, 117406. https://doi.org/10.1016/j.carbpol.2020.117406.
4. Lusic, H.; Grinstaff, M. W. X-Ray-Computed Tomography Contrast Agents. Chem. Rev. 2013, 113 (3), 1641–1666. https://doi.org/10.1021/cr200358s.

CONTACTS

You are welcome to contact any of the API Professors:

Mark Martinez
Professor, UBC
604-822-8564
Mark.Martinez@ubc.ca

James Olson
Professor, UBC
604-822-5705
James.Olson@ubc.ca

Rodger Beatson
Professor, BCIT
604-432-8951
Rodger_Beatson@bcit.ca